# nature communications



**Article** 

https://doi.org/10.1038/s41467-025-63618-5

# Enriching conductive capping by alkaline treatment of perovskite quantum dots towards certified 18.3%-efficient solar cells

Received: 6 February 2025

Accepted: 25 August 2025

Published online: 29 September 2025

Check for updates

Donglin Jia<sup>1</sup>, Jiaxin Li<sup>1</sup>, Kefan Zhu<sup>1</sup>, Hengwei Qiu<sup>1</sup>, Liang Li<sup>1</sup>, Xing Zhao<sup>1</sup>, Zhineng Lan<sup>1</sup>, Huilin Yan<sup>1</sup>, Fu Yang<sup>1</sup>, Peng Cui <sup>1</sup>, Xin Sun<sup>1</sup>, Haifang Li<sup>1</sup>, Pengkun Zhu<sup>1</sup>, Shaofeng Liu<sup>2</sup> & Meicheng Li <sup>1</sup>□

Perovskite quantum dots (PQD) hold great promise for next-generation photovoltaics. However, neat ester antisolvents hydrolyze inefficiently into target ligands under ambient conditions, compromising the formation of integral conductive capping on PQD surfaces. Herein, we construct alkaline environments, which facilitate the rapid substitution of pristine insulating oleate ligands with up to twice the conventional amount of hydrolyzed conductive counterparts. Theoretical calculations reveal that this environment renders ester hydrolysis thermodynamically spontaneous and lowers reaction activation energy by approximately 9-fold. Through tailoring potassium hydroxide coupled with methyl benzoate antisolvent for interlayer rinsing of PQD solids, the assembled light-absorbing layers exhibit fewer trap-states, homogeneous orientations, and minimal particle agglomerations. Consequently, the fabricated solar cells (0.036 cm<sup>2</sup>) achieve a certified efficiency of 18.3%, the highest value among published PQD solar cell reports, alongside a steady-state efficiency of 17.85% and an average efficiency of 17.68% over 20 devices. Moreover, the alkaline treatment is broadly compatible with diverse solid-state treatments and PQD compositions, demonstrating universality in modulating PQD surface chemistry.

Solution-processed lead halide perovskite quantum dots (PQD) have garnered substantial research interest in light-emitting diodes (LED)<sup>1-3</sup>, photodetectors<sup>4</sup>, lasers<sup>5</sup>, and photovoltaics<sup>6-8</sup>, owing to their tunable bandgap energy ( $E_{\rm g}$ ), high photoluminescence quantum yields (PLQY), defect tolerance, and chemical processability<sup>9-11</sup>. In particular, lead iodide PQDs (APbI<sub>3</sub> PQD, A=cesium (Cs<sup>+</sup>), methylammonium (MA<sup>+</sup>), or formamidinium (FA<sup>+</sup>)) are promising for next-generation solar cells due to their high light absorption coefficients ( $10^5$  cm<sup>-1</sup>) and  $E_{\rm g}$ s closer to the ideal Shockley-Queisser theoretical value (-1.34 eV). Compared to bulk counterparts, the enhanced surface strain of PQDs with a large surface-to-volume ratio stabilizes their perovskite core lattices in the

photoactive black phase<sup>12</sup>. Meanwhile, the colloidal synthesis of PQDs separates their crystal growth from film deposition, enabling device manufacturing processes to be more tolerant of environments<sup>13–15</sup>. Continued advances in surface ligand chemistry, A-site composition regulation, and homo-/hetero-junction light-absorbing layer architecture design have significantly improved the power conversion efficiency (PCE) of PQD solar cells (PQDSC) from 10.7% to the currently National Renewable Energy Laboratory (NREL) certified 19.1%<sup>16–21</sup>. In particular, benefiting from suitable Goldschmidt tolerance factors, long exciton lifetimes, and tailorable lattice structures, hybrid A-site lead iodide PQDs prepared by post-synthetic cation exchange enable

<sup>1</sup>State Key Laboratory of Alternate Electrical Power System with Renewable Energy Sources, School of New Energy, North China Electric Power University, Beijing, China. <sup>2</sup>State Key Laboratory of Precision Measurement Technology and Instruments, Department of Precision Instrument, Tsinghua University, Haidian, Beijing, China. —e-mail: mcli@ncepu.edu.cn

solar cell devices exhibiting higher short-circuit current ( $J_{SC}$ ) and lower open-circuit voltage ( $V_{OC}$ ) deficits<sup>22–24</sup>.

The light-absorbing layer of a PODSC is typically assembled by the layer-by-layer deposition of POD solid films, with each layer rinsed using an antisolvent of appropriate polarity to adequately remove the pristine ligands from the POD surface without disrupting or dissolving the perovskite core, thereby benefiting subsequent solution depositions<sup>6,25-27</sup>. Wheeler et al. revealed that the pristine long-chain oleate (OA) ligands on the X-site of PQD surface could be substituted by short acetate (Ac<sup>-</sup>) ligands hydrolyzed from methyl acetate (MeOAc) antisolvent under ambient humidity, improving charge transfer between adjacent PQDs<sup>28</sup>. Since then, esters have been commonly used antisolvents for interlayer rinsing of PQD solid films. Upon achieving the desired thickness, post-treatment with alternative short cationic ligands (such as FA+, phenethylammonium (PEA+), and the lately reported MA<sup>+</sup>) to substitute the pristine long-chain oleylammonium (OAm+) ligands on the A-site of PQD surface could further enhance electronic coupling of inter-PQDs, thereby resulting in PQDSCs with advanced performance<sup>29-31</sup>. Our previous study identified protic 2-pentanol (2-PeOH) with moderate polarity as the ideal solvent of cationic salts, which mediated efficient A-site ligand exchange during post-treatment of PQD solid films32. Recent development of concentrated quantum dot inks (≥200 mg mL<sup>-1</sup>) via liquid-state ligand exchange has demonstrated promising scalability, enabling the singlestep deposition of light-absorbing layers with enough thickness and conductivity<sup>7,8</sup>. However, the inherent fragility of the ionic perovskite lattice imposes limitations on selecting solvents for PQDs after ligand exchange, which prevents the application of sufficiently short ligands with high polarity, thus compromising the efficiency of resulting PQDSCs.

Despite the progress achieved in enhancing the photovoltaic efficiency of PQDSCs through regulating A-site cationic ligand salts for post-treatment, the controlled solubilization of highly polar exogenous anionic salts in mild ester antisolvents remains challenging for interlayer ligand exchange. As a result, relying on ambient hydrolysis of ester antisolvents to generate target anionic ligands has become the standard practice to exchange the X-site pristine OA ligands during interlayer rinsing of PQD solids33. Nevertheless, the robust C-O-CH3 bonding of esters hinders their hydrolysis spontaneity. Hence, conventional neat ester antisolvent rinsing predominantly induces the direct dissociation of dynamically bound pristine OA ligands rather than substituting them with hydrolyzed shorter counterparts, thereby generating extensive surface vacancy defects to capture carriers<sup>34</sup>. Moreover, Ac ligands hydrolyzed from traditional MeOAc antisolvent exhibit weak binding to the PQD surface, challenging to provide a durable capping for ensuring effective charge transfer35. Importantly, if the removed pristine X-site anionic ligands are not effectively replenished by the alternatives during the interlayer antisolvent rinsing process, the surfaces of these PQDs would be destabilized. As a result, undesirable aggregation would occur from further shrinkage of interparticle space during subsequent A-site cationic ligand exchange, which in turn deteriorates charge transport of the assembled lightabsorbing layers. Therefore, identifying esters with appropriate functional groups and controllably enhancing their hydrolysis probability are essential for effective interlayer antisolvent rinsing, which allows the dynamically bound pristine long-chain insulating OA ligands to be sufficiently substituted with robustly bound short conductive ligands, highly desirable for further enhancing the photovoltaic performance and stability of PQDSCs.

Herein, an alkali-augmented antisolvent hydrolysis (AAAH) strategy is presented to improve the conductive capping of PQD surface, supported by comprehensive theoretical calculations and experimental studies. The investigation of esters with different functional groups identified methyl benzoate (MeBz) with suitable polarity as the preferred antisolvent for interlayer rinsing of PQD solid films, and its

hydrolyzed ligands enable superior binding and charge transfer properties on the POD surface. Notably, the establishment of alkaline environments significantly overcame both the thermodynamic spontaneity and kinetic activation energy barriers to ester hydrolysis. thereby enabling the rapid formation of short anionic ligands that effectively substituted the pristine long-chain OA ligands during interlayer antisolvent rinsing. Through carefully regulating the alkalinity, potassium hydroxide (KOH) was screened to ensure adequate ligand exchange without compromising the structural integrity, resulting in a conventional 2-fold number of densely conductive short ligands capping on the PQD surface. Consequently, the fabricated hybrid FA<sub>0.47</sub>Cs<sub>0.53</sub>PbI<sub>3</sub> PQDSCs yielded a remarkable PCE of 18.37% (certified 18.30%), the highest value among hybrid A-site PQDSCs. Moreover, the storage and operational stability of solar cells were both improved. Charge carrier dynamics revealed that the high photovoltaic performance was attributed to the assembly of light-absorbing layers with fewer defects, homogeneous crystallographic orientations, minimal PQD agglomerations, and favorable energy level positions through the AAAH strategy, resulting in suppressed trap-assisted recombination and facilitated charge extraction within PQDSCs.

#### Results

#### Neat ester antisolvent rinsing of PQD solids

The hybrid FA<sub>0.47</sub>Cs<sub>0.53</sub>Pbl<sub>3</sub> PQDs with an average size of -12.5 nm and photoluminescence (PL) emission peak at 728 nm were prepared via post-synthetic cation exchange of CsPbl<sub>3</sub> PQD parent according to our previous report (Supplementary Fig. 1)<sup>36</sup>. The resulting PQD colloids were spin-coated into solid films for subsequent analysis.

Esters are regarded as an available antisolvent for interlayer rinsing PQD solid films because they possess neither protonicity nor nucleophilicity, which ensures both the removal of dynamically bound pristine long-chain ligands and avoids attacking the perovskite core, thus favoring deposition of subsequent layers<sup>37</sup>. Meanwhile, the pristine long-chain insulating OA ligands on the PQD surface have the potential to be exchanged by the short conductive acidic anions hydrolyzed from esters<sup>27</sup>. Therefore, starting with the viewpoint concerning functional groups of the anionic ligands bound to the X-site of POD surface, we first investigated the effect of neat ester antisolvents rinsing on the performance of PQDs and corresponding solar cell devices<sup>38</sup>. Effective ester antisolvents for rinsing PQD solid films should foremost meet these criteria: (1) high hydrolysis probability; (2) hydrolysis to short ligands; (3) rapid and efficient removal after rinsing. To meet the above requirements, esters that possess short hydrocarbon chain lengths at both the acyl and alcohol ends were preferred, which minimizes the spatial resistance for water molecule adhesion while ensuring low viscosity and boiling point for uniform coverage and rapid evaporation. Therefore, listed in decreasing order of polarity, esters including methyl methanesulfonate (MMS), methyl benzenesulfonate (MeBzSO<sub>3</sub>), methyl formate (MeFo), ethyl formate (EtFo), MeOAc, MeBz, ethyl acetate (EtOAc), and ethyl cinnamate (EtCa), were selected for rinsing PQD solid films (Supplementary Fig. 2 and Supplementary Table 1).

In our typical experiments, a preliminary screening of alternative antisolvents was carried out. Initially, an "as-cast" solid film of PQDs covered with pristine OA- and OAm<sup>+</sup> ligands was prepared, followed by rinsing it with alternative antisolvents under ambient conditions at a relative humidity (RH) of -30%. This step was designed to initiate hydrolysis with atmospheric moisture, thereby substituting the pristine OA<sup>-</sup> ligands with the generated acidic anions. The resulting PQD solid films are hereafter referred to as "antisolvent-based" samples. As shown in Fig. 1a, despite sulfonates being widely reported as efficient capping agents on account of their strong binding affinity to perovskites, rinsing with either sulfonate-based ester in our study led to the instantaneous and complete degradation of the perovskite core. Moreover, as shown in Supplementary Fig. 3, among

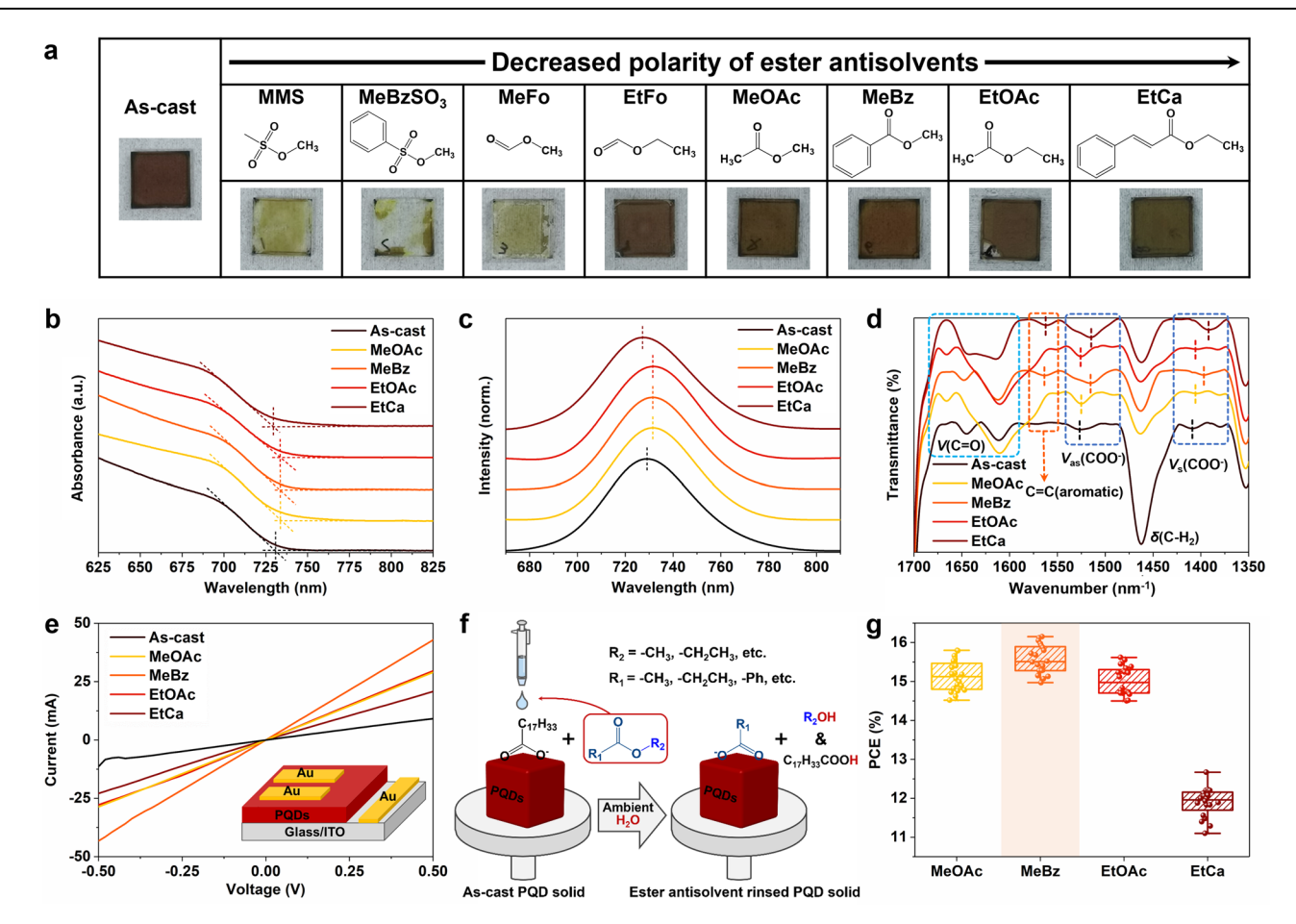


**Fig. 1** | **Effects of neat ester antisolvent treatment on PQDs. a** Molecular structures of the alternative ester antisolvents used in this work. Light absorption spectra (**b**), normalized PL spectra (**c**), FT-IR spectra (**d**), and conductivity (**e**) of ascast, MeOAc-, MeBz-, EtOAc-, and EtCa-based PQD solid films. The Inset in (**e**) shows

the device architecture for conductivity measurement. **f** Schematic illustration of ligand exchange during ester antisolvent rinsing of PQD solid films. **g** PCE statistics of MeBz-, EtOAc-, and EtCa-based PQDSCs. For each condition, 20 devices fabricated from different batches were applied for statistics.

carboxylate-based esters, the excessive polarity of MeFo and EtFo resulted in degradation and film cracking of the assembled PQDs, respectively. In contrast, rinsing with ester antisolvents of moderate polarity, such as MeOAc, MeBz, and EtOAc, preserved the structural integrity of PQD solids, leading to denser packing without the formation of visible cracks. Notably, the EtCa-based PQD solid exhibited a rougher and more porous morphology, accompanied by a less ordered packing arrangement. Therefore, in the following, we focused on discussing the effect of these available ester antisolvents on the properties of PQDs.

Figure 1b, c present the light absorption and steady-state photoluminescence (PL) spectra of PQD solid films, and the corresponding Tauc plots are shown in Supplementary Fig. 4a. It can be observed that compared to the as-cast sample. POD solid films rinsed with MeOAc. MeBz, and EtOAc show the identical extent of red-shifted spectra, indicating improved electronic coupling of inter-PQDs<sup>39</sup>. In contrast, PQD solid film treated by EtCa exhibited a slight blue-shifted emission compared to the as-cast sample. This is likely attributed to the disrupted pristine crystallographic orientation caused by surface strain, which arises from the hydrolyzed cinnamate anionic ligands with rigid and bulky conjugated benzene rings and alkenyl groups (Supplementary Fig. 4b, c)<sup>40</sup>. Fourier-transform infrared (FT-IR) spectra of PQD solid films were measured to monitor the status of surface ligands. As shown in Fig. 1d, ester antisolvent treatments significantly weakened the alkyl stretching vibrational signals of PQDs, including  $v(C-H_2)$  at 1460 cm<sup>-1</sup>,  $v(C-H_x)$  at 2780–2980 cm<sup>-1</sup>, and v(C=C-H) at 3005 cm<sup>-1</sup>, indicating removal of pristine long-chain oleyl ligands. In contrast, the stretching vibration strengths of ammonium and imine groups (v(N- $H_3^+$ ) at 3138 cm<sup>-1</sup> and  $v(C = N \cdot H_2^+)$  at 3200-3450 cm<sup>-1</sup>) were almost identical in all samples, suggesting the pristine OAm+ ligands and FA+ cations on PQD surface were essentially unaffected after ester antisolvent treatments (Supplementary Fig. 4d). Notably, all PQDs rinsed with ester antisolvents exhibited stronger C = O stretching vibration centered at 1636 cm<sup>-1</sup> compared to the as-cast sample<sup>41</sup>. These observations suggest changes in the chemical environment of carboxylate groups on the PQD surface after being rinsed by esters, probably resulting from the substitution of pristine OA ligands with other species containing carboxylate groups. In addition, MeBz- and EtCa-based PQDs show distinctive aromatic C = C bending vibrational modes at 1562 cm<sup>-1</sup>, and the carboxylate stretching vibration signals ( $v_s(COO^{-1})$ around 1400 cm<sup>-1</sup> and  $v_{as}(COO^{-})$  around 1520 cm<sup>-1</sup>) were shifted toward lower wavenumbers in these two samples compared to others. likely due to the conjugation effects from benzene and vinyl groups<sup>42</sup>. We proceeded to study the resistance of PQD solid films. Vertical conductivity combined with film thickness measurements (Fig. 1e and Supplementary Fig. 5) revealed that all ester antisolvent-rinsed PQDs exhibited markedly enhanced conductivity compared with their ascast state, whose surfaces remained densely covered by pristine longchain insulating ligands<sup>33</sup>. Among these, the MeBz-based PQDs possessed the highest conductivity, ~1.5 times higher than that of conventional MeOAc- and EtOAc-rinsed PQDs, whereas the conductivity of PQDs rinsed by EtCa with a longer hydrocarbon chain was weaker, at only ~53% of MeBz-based PQDs. These results indicated that ester antisolvents with different functional groups at the acyl ends have the

potential to hydrolyze into various acetic anions under ambient moisture to substitute the pristine long-chain OA' ligands during the rinsing process. The lengths of these functional groups determine the coupling degree of inter-PQDs, while their electronic properties determine the binding status of the hydrolyzed anionic ligands on the PQD surface, as illustrated in Fig. 1f.

Subsequently, we investigated the effect of neat ester antisolvent treatments on the photovoltaic performance of PQDs by fabricating solar cell devices. During the preparation of the light-absorbing layer, PQD solid films underwent solely interlayer rinsing with the aforementioned ester antisolvents, without any additional treatments. Figure 1g and Supplementary Fig. 6 present the statistical PCEs and other parameters, including  $V_{OC}$ ,  $J_{SC}$ , and fill factor (FF) of these PQDSCs derived from 20 devices manufactured across different batches. The corresponding data are summarized in Supplementary Table 2. MeBz-based PQDSCs show an average PCE of 15.57%, surpassing those of the conventional MeOAc- and EtOAc-based devices. In contrast, despite the advantage of more conjugated Π-bonds favoring electron transport, employing EtCa with a longer hydrocarbon chain for rinsing PQD solid films significantly rolled off the FF and efficiency of solar cells. The efficiency trends of solar cells paralleled the conductivities of corresponding PQD solid films, highlighting the importance of enhancing charge transport between PQDs to achieve PQDSCs with high photovoltaic performance.

Therefore, to thoroughly investigate the reason for MeBz enhancing the optoelectronic properties of PQDSCs, we conducted density functional theory (DFT) calculations. Coordinates of ligand-bound surface models are provided in Supplementary Data 1. Our results revealed that the benzoate (BZA') anionic ligands hydrolyzed from MeBz exhibit stronger binding affinity and electron transfer capability to the PQD surface compared to the Ac ligands hydrolyzed from conventional MeOAc (Supplementary Fig. 7), confirming its suitability as the target anionic ligand<sup>43</sup>. Although MeBz rinsing improved the photovoltaic performance of PQDSCs, the X-ray photoelectron spectroscopy (XPS) analysis indicated that chemical environments of POD surface deteriorated after both the conventional neat MeOAc and the preferred neat MeBz rinsing compared to the as-cast state (Supplementary Fig. 8). This primarily resulted from the incomplete ligand capping on these rinsed PQD surfaces, suggesting that neat antisolvent rinsing predominantly drives the direct dissociation of pristine ligands, thereby compromising carrier transport and the stability of the PQDs. Therefore, it is imperative to increase the hydrolysis probability of ester antisolvents to achieve more adequate short ligand compensation.

# Ligand exchange of PQDs based on alkali-augmented antisolvent hydrolysis

For the accomplishment of adequate ligand exchange, we introduced a series of alkaline additives, including NaOH, KOH, Me<sub>3</sub>SiOK, and  $K_2CO_3$ , in descending order of alkalinity, into the ester to prepare saturated solutions, thereby promoting ester hydrolysis through controlled modulation of the alkaline environment. The rationale for specific alkalis added into the antisolvent is presented in Supplementary Note 1. Given that MeBz demonstrated superior potential to other esters listed above for enhancing the performance of PQDSCs, herein, we focused on investigating the properties of MeBz antisolvents and MeBz-based PQDs.

Firstly, the pH values of the regulated antisolvents were tested, showing about 6.7 for neat MeBz, which increased progressively with the alkalinity of the added alkali (quantitative data are provided in Supplementary Fig. 9). The as-cast PQD films were then rinsed with these antisolvents, and the resulting samples were designated as "MeBz/alkali-based". Unfortunately, NaOH with excessively high alkalinity could attack PQD surface components via strong hydrogen bonds, resulting in the disintegration and decomposition of the solid

film (Supplementary Fig. 10). In contrast, MeBz with added other alkalis did not visibly damage the PQD solid film. As shown in Fig. 2a, we proceeded to measure the X-ray diffraction (XRD) pattern of PQD solid films rinsed with MeBz containing the available alkalis and found that the diffraction peak position, intensity, and full width at half-maximum (FWHM) of these samples remained almost constant, indicating the crystal structure and grain size of PQDs were unaffected. Therefore, we will mainly discuss the surface properties of PQDs in the following. After identifying the available alkaline additives, we designed and conducted hydrolysis experiments (detailed procedures and analyses are provided in Supplementary Fig. 11 and Supplementary Note 2) and confirmed that their ability to promote MeBz hydrolysis increases with their alkalinity.

As illustrated in the FT-IR spectra (Fig. 2b), when the alkalinity of the added additive did not exceed that of KOH, rinsing PQD solid films with MeBz/alkali antisolvents would not introduce destructive hydroxyl groups (stretching vibration mode at 3250–3600 cm $^{-1}$ ) to the PQD surface. Notably, we observed that the  $v_{\rm s}({\rm COO}^{-1})$  signal in PQDs rinsed with MeBz/alkali antisolvents shifted toward higher wavenumbers of 1408 cm $^{-1}$  compared to the sample rinsed with neat MeBz (1399 cm $^{-1}$ ), with increasing intensities correlating with the alkalinity of the added alkalis. Correspondingly, the intensity of the C = C stretching peak at ~1468 cm $^{-1}$  in the Raman spectra, originating from the benzene ring of PQDs, was also stronger with increasing pH values of the MeBz/alkali antisolvents used for rinsing PQD solid films (Supplementary Fig. 12) $^{+4}$ . These observations indicate an increased presence of deprotonated BZA species on the surface of MeBz/alkali antisolvents rinsed PQDs, likely interacting closely with the uncoordinated Pb $^{2+}$ .

The <sup>1</sup>H nuclear magnetic resonance (NMR) spectra detailed the status of ligands on the PQD surface, as depicted in Fig. 2c and Supplementary Fig. 13a. To avoid the proton signal overlapping between the amidinium group of FA<sup>+</sup> cation and the aromatic group of MeBz, we chose CsPbI<sub>3</sub> PQDs as the sample for NMR measurement, instead of FA<sub>v</sub>Cs<sub>1-v</sub>PbI<sub>3</sub> PQDs. Samples were prepared by scraping PQD powders from Si wafers and dissolving them completely in deuterated chloroform (d-CDCl<sub>3</sub>) at a concentration of 2 mg mL<sup>-1</sup>. Compared to the sample rinsed with conventional MeOAc (Supplementary Fig. 13b), PQDs treated by MeBz exhibited distinct aromatic proton resonances originating from phenyl groups (para protons H<sub>a</sub>, meta protons H<sub>b</sub>, and ortho protons H<sub>c</sub>) with chemical shifts (δ) ranging from 7.4 to 8.2 ppm. These resonances were sharpened and downfield-shifted relative to the corresponding resonances of neat MeBz, confirming the hydrolyzed BZA ligands were robustly bound to the uncoordinated Pb<sup>2+</sup> on the PQD surface via electron donation<sup>45</sup>. Furthermore, each <sup>1</sup>H NMR peak was normalized to the intensity of the chloroform proton resonance ( $\delta$  = 7.26 ppm) for quantitative analysis of phenyl groups on the MeBz-rinsed PQD surface, with the content increasing with the alkalinity of the added alkali, suggesting that compensation of short ligands hydrolyzed from MeBz on the PQD surface vacancies was effectively enhanced. Particularly, MeBz/KOH-based PQDs possessed the largest number of BZA ligands, up to twice that of the neat MeBzbased sample. As shown in Fig. 2d and Supplementary Fig. 14, further analysis of the XPS spectra of PQD solid films revealed that, in comparison to the neat MeBz-based PQDs, despite no variation in the composition of perovskite core (Supplementary Table 3), the Pb 4f peaks of samples rinsed with MeBz/alkali antisolvents shifted towards lower binding energies, indicative of electron acquisition<sup>46</sup>. Furthermore, the ratio between carboxyl groups (~532.5 eV) and hydroxyl groups (-531.4 eV) in samples increased with the pH value of the rinsed MeBz/alkali antisolvent, corresponding to a gradual reduction in anionic vacancies on the PQD surface<sup>11</sup>. Notably, no signal of the K element was detected among these samples. Therefore, based on the combined results of FT-IR, NMR, and XPS analyses, we conclude that the AAAH strategy effectively compensates for X-site vacancies on the PQD surface by introducing a greater number of short anionic ligands

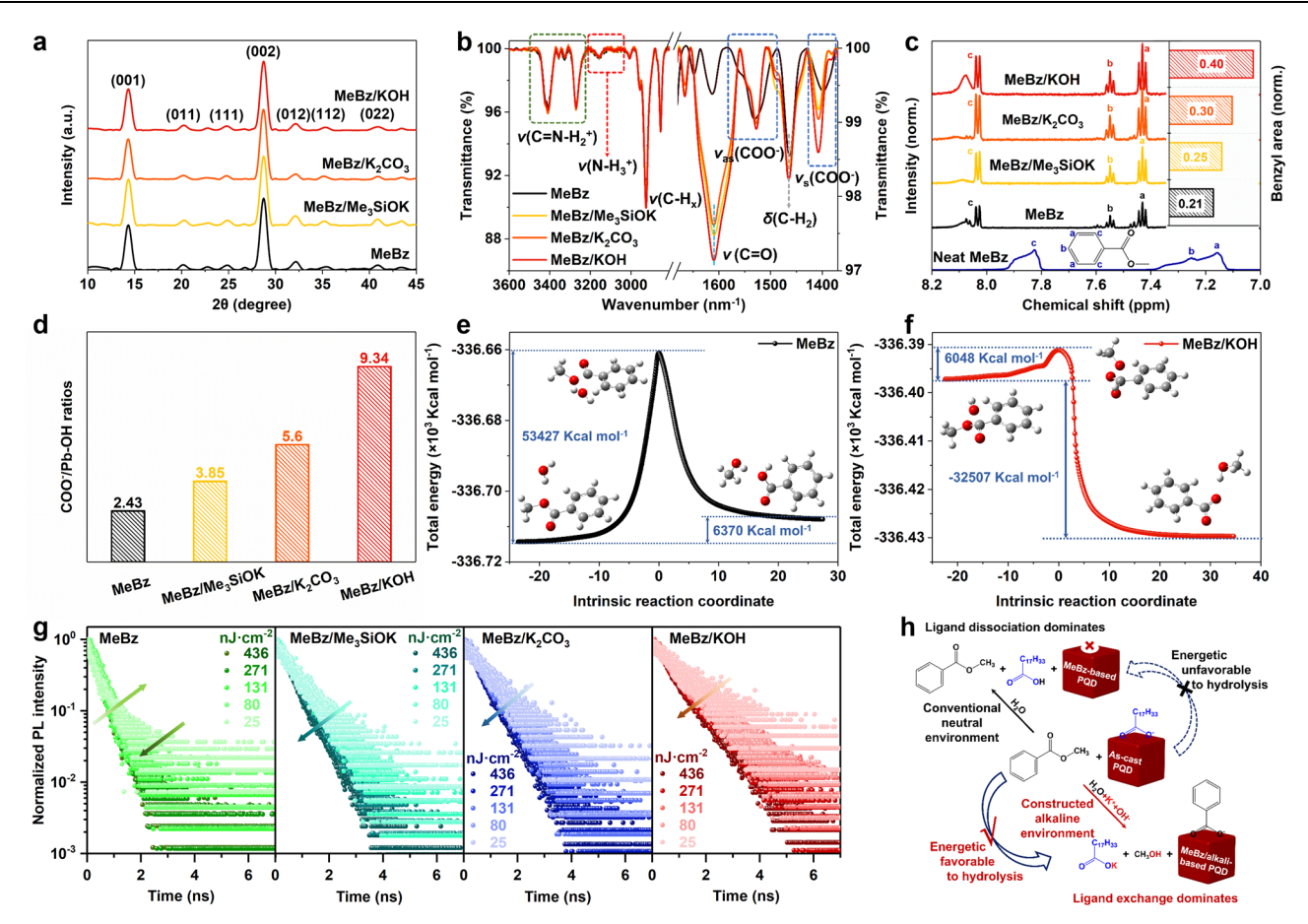


**Fig. 2** | **Effects of AAAH strategy on ligand exchange of PQDs.** XRD pattern (a), FT-IR spectra (b),  ${}^{1}$ H NMR spectra (c), and histograms of carboxyl-to-hydroxyl group ratios (d) for MeBz-, MeBz/K<sub>2</sub>CO<sub>3</sub>-, MeBz/Me<sub>3</sub>SiOK-, and MeBz/KOH-based PQD solid films. Note that in (b), spectral ordinates on the left and right sides of the dividing line correspond to their respective transmittance ranges. Changes in  $\Delta G$ 

values for MeBz hydrolysis in conventional neutral (e) and constructed alkaline (f) environments, referenced to the initial state of each system. g Fluence-dependent TRPL spectra of MeBz-, MeBz/K<sub>2</sub>CO<sub>3</sub>-, MeBz/Me<sub>3</sub>SiOK-, and MeBz/KOH-based PQD solid films. h Schematic comparison diagram of conventional and AAAH-based ligand exchange of PQDs using MeBz antisolvent.

hydrolyzed from ester antisolvents, rather than anions or cations dissociated from the added alkalis.

First-principles calculations were conducted to identify the transition state (TS) of MeBz hydrolysis, providing a theoretical study of the reaction process (Supplementary Fig. 15), according to the following reaction Eqs. 1 and  $2^{47}$ ,

$$C_6H_5COOCH_3 + H_2O \rightarrow C_6H_5COOH + CH_3OH \tag{1}$$

$$C_6H_5COOCH_3 + OH^- \rightarrow C_6H_5COO^- + CH_3OH$$
 (2)

As illustrated in Fig. 2e and Supplementary Movie 1, the calculated total energy of products was higher than that of reactants, indicating that the conventional ester hydrolysis reaction requires absorbing sufficient external thermal energy to realize. Additionally, the activation energy ( $E_a$ ) for MeBz hydrolysis in a neutral environment was as high as 53427 Kcal mol<sup>-1</sup>, reflecting a slow rate of the hydrolysis reaction. Despite evidence that the PQD surface functions as an active site for catalyzing chemical reactions, simultaneously overcoming both thermodynamic and kinetic barriers for MeBz hydrolysis remains a significant challenge<sup>48</sup>. In contrast, Fig. 2f and Supplementary Movie 2 demonstrate that the introduction of hydroxide ions (OH) into the reaction system substantially decreased the total energy difference between reactants and products, signifying that the MeBz hydrolysis reaction becomes highly spontaneous at room temperature.

Furthermore, the  $E_{\rm a}$  for MeBz hydrolysis was reduced to 6048 Kcal mol<sup>-1</sup>, triggering a faster reaction rate. These results indicate that the alkaline environment effectively lowers the energy threshold for MeBz hydrolysis, contributing to the rapid generation of more short-cationic ligands.

To examine the effect of the constructed hydrolysis environment for ester antisolvents on the photophysical properties of PQDs, we performed light absorption, steady-state PL, and time-resolved PL (TRPL) measurements on PQD solid films, as shown in Supplementary Fig. 16. No notable distinctions in the absorption edge and PL peak positions were found among samples rinsed with different MeBz/alkali antisolvents, indicating that the  $E_{\rm g}$  of PQDs was not affected. However, the PL intensity and lifetime of these samples increased with the pH value of the employed MeBz/alkali antisolvent. To in-depth analyze the carrier dynamics within PQD solids, fluence-dependent TRPL measurements were performed under confocal excitation. As shown in Fig. 2g, the PL lifetime of the neat MeBz-based PQD solid exhibited an initial increase as the excitation fluence increased from 25 to 80 nJ·cm<sup>-2</sup>, followed by a decrease at higher fluences. This suggests that a trap-assisted Shockley-Read-Hall recombination dominates at low fluence, which transits to bimolecular radiative recombination once the traps become saturated upon photon filling<sup>49</sup>. In contrast, all three MeBz/alkali-based samples exhibited monotonic decreases in their carrier lifetimes with increasing fluence, which is consistent with a regime dominated by radiative recombination with lower trap density<sup>34</sup>. Among these samples, MeBz/KOH-based PQDs consistently

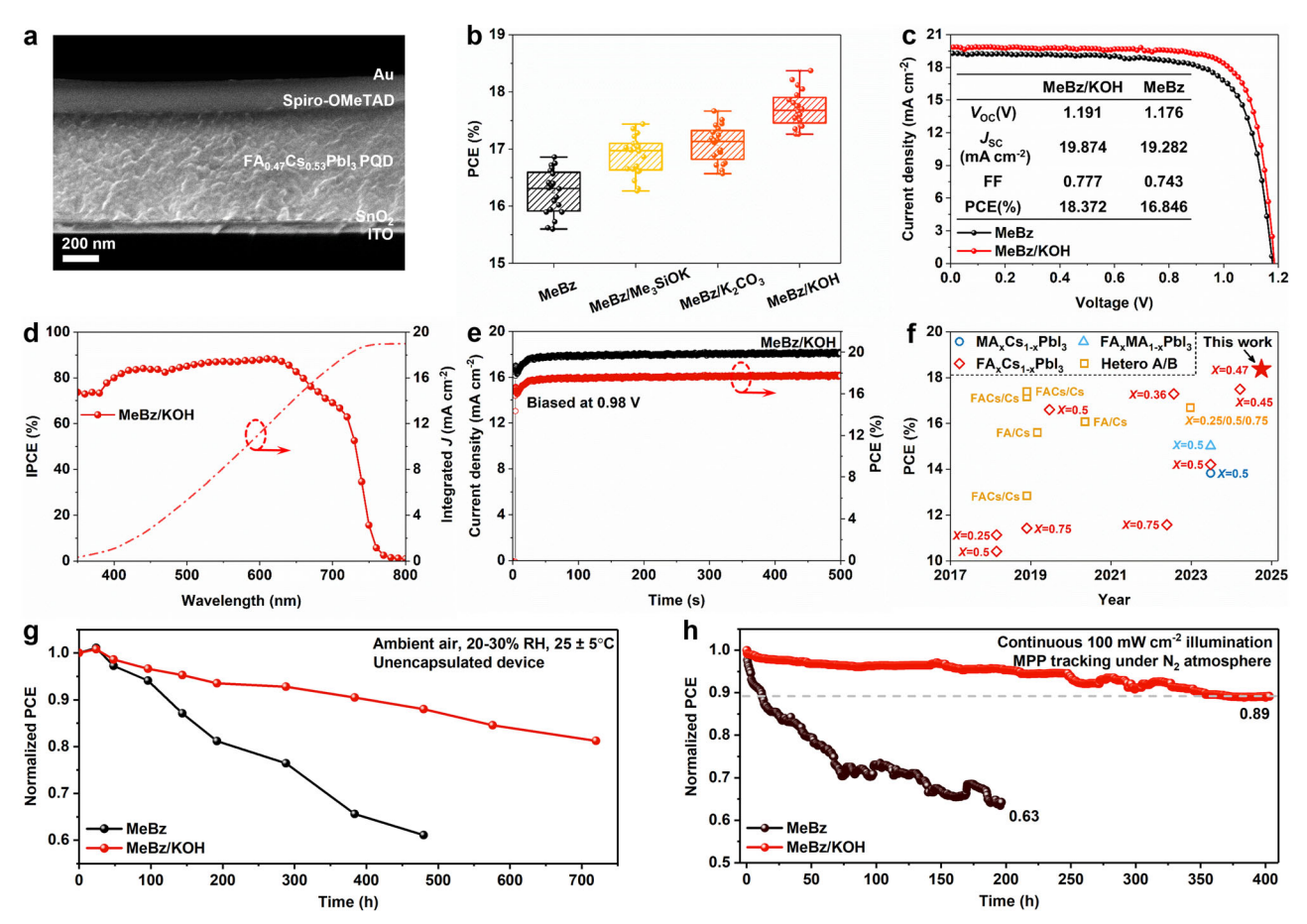


**Fig. 3** | **Effects of AAAH strategy on photovoltaic performance of PQDSCs. a** Cross-sectional SEM image of a FA<sub>0.47</sub>CS<sub>0.53</sub>Pbl<sub>3</sub> PQDSC device. **b** Statistical PCEs of MeBz-, MeBz/K<sub>2</sub>CO<sub>3</sub>-, MeBz/Me<sub>3</sub>SiOK- and MeBz/KOH-based PQDSCs. For each condition, 20 devices fabricated from different batches were applied for statistics. **c** *J–V* curves of MeBz- and MeBz/KOH-based PQDSCs. IPCE spectrum (**d**) and

stabilized PCE (e) of the MeBz/KOH-based PQDSC. f Evolution of reported PCEs for hybrid A-site PQDSCs with publication year. Stability of the unencapsulated MeBz-and MeBz/KOH-based PQDSCs under ambient conditions of  $25\pm5\%$  RH storage (g), and continuous 100 mW cm<sup>-2</sup> white LED illumination in an  $N_2$  atmosphere (h).

showed the longest PL lifetime across all excitation fluences, indicating the lowest trap density, followed by MeBz/ $K_2CO_3$ - and MeBz/ $Me_3SiOK$ -based samples, while neat MeBz-based PQDs exhibited the shortest lifetime. Supplementary Tables 4 and 5 summarize the fitting parameters of TRPL decay curves using phenomenological models. Although these models were not necessarily physically relevant, they primarily provided a numerical description of the PL decay process. It can be found that the variation trends in carrier lifetime closely correlate with the PL intensity order of these PQDs, confirming that the AAAH-based ligand exchange leads to more effective surface ligand capping, with KOH emerging as the most effective additive among those tested.

Based on the aforementioned results, we summarized the impact of the AAAH strategy on the ligand exchange and photophysical properties of PQDs, as illustrated in Fig. 2h. When neat MeBz is used as an antisolvent for rinsing PQD solid films, the requirement for external energy input and the high  $E_{\rm a}$  combine to hinder its hydrolysis in neutral environments at room temperature. Consequently, the dynamically bound pristine long-chain OA ligands are predominantly dissociated from the PQD surface rather than substituted by short anionic counterparts during rinsing. Although this improves the conductivity of inter-PQDs, it introduces numerous surface vacancy defects, potentially deteriorating the photophysical properties of PQDs. In contrast, the AAAH strategy involves the introduction of alkalis into MeBz, successfully overcoming the substantial thermodynamic and kinetic barriers to ester hydrolysis by constructing an appropriate alkaline

environment. This allows the pristine long-chain OA ligands to be substituted by up to twice the conventional number of shorter BZA ligands during the brief antisolvent rinsing process, thereby ensuring the integrity of conductive termination on PQD surface, effectively enhancing charge transport between PQDs and avoiding the formation of surface trap states.

# Photovoltaic performance of PQDSCs

To study the effect of optimizing the environment for antisolvent hydrolysis on the photovoltaic performance of PQDs, we constructed PQDsCs with indium-doped tin oxide (ITO)/tin dioxide (SnO<sub>2</sub>)/PQDs/2,2',7,7'-tetrakis[N,N-bis(4-methoxyphenyl)amino]-9,9'-spirobi-

fluorene (Spiro-OMeTAD)/Au planar structures. Figure 3a shows the cross-sectional scanning electron microscopy (SEM) image of the asfabricated PQDSC device, where SnO<sub>2</sub> and Spiro-OMeTAD films serve as the electron and hole transport layers (ETL and HTL), respectively. To maximize the efficiency of fabricated PQDSCs, the layer-by-layer assembled PQD solid film, acting as the light-absorbing layer, was further post-treated with a 2-PeOH solution of short cationic ligands (named 2-PeOH/ligand) to sufficiently exchange the pristine long-chain OAm<sup>+</sup> ligands, as previously reported<sup>32</sup>. The detailed description is provided in the Methods. The photovoltaic performance of PQDSCs was evaluated under AML5 G 100 mW cm<sup>-2</sup> illumination. We first compared various cationic ligands for the post-treatment of PQD solid films, including previously reported FA<sup>+29</sup>, PEA<sup>+31</sup>, choline (CH<sup>+</sup>)<sup>32</sup>, trimethylsulfonium (TMS<sup>+</sup>)<sup>13</sup>, and other alternative candidates, by

measuring the efficiencies of fabricated PQDSCs (Supplementary Fig. 17 and Supplementary Table 6), and concluded that the benzamidinium (PhAD<sup>+</sup>), simultaneously containing a conjugated benzene ring and a FA<sup>+</sup> cation, ensured favorable surface charge transport and binding affinity with the surface A-site of FA<sub>0.47</sub>Cs<sub>0.53</sub>PbI<sub>3</sub> PQDs. Figure 3b shows the statistical PCEs of PQDSCs fabricated with 2-PeOH/PhAD<sup>+</sup> post-treatment, with the corresponding photovoltaic parameters, including  $V_{OC}$ ,  $J_{SC}$ , and FF, summarized in Supplementary Fig. 18 and Supplementary Table 7. It can be observed that all devices demonstrated high reproducibility, with efficiency increasing with the pH value of the employed MeBz/alkali antisolvent. This trend was duplicated in PQDSCs fabricated without post-treatment (Supplementary Fig. 19 and Supplementary Table 8). Notably, MeBz/KOHbased PQDSCs exhibited markedly superior photovoltaic performance compared to devices fabricated with other MeBz/alkali-based PQDs, indicating that the combination of MeBz with KOH is the preferred antisolvent for rinsing the PQD interlayer. Consequently, we focus primarily on a comparative study between MeBz- and MeBz/KOHbased PQDSCs in the following.

As demonstrated by the photocurrent density-voltage (J-V) curves of the champion devices (Fig. 3c), the MeBz-based PQDSC yielded a PCE of 16.85% with a  $V_{\rm OC}$  of 1.162 V and an FF of 0.745. In contrast, MeBz/KOH-based PQDSCs achieved improved  $V_{
m OC}$  and FF values of 1.194 V and 0.775, respectively, resulting in a PCE as high as 18.37%. Moreover, the best-performing MeBz/KOH-based PQDSC was certified by an independent solar cell accreditation laboratory, obtaining a PCE as high as 18.30% (Supplementary Fig. 20), which is the highest certified efficiency among published PQDSC reports to date, as summarized in Supplementary Table 9. Despite observing a slight hysteresis phenomenon when recording J-V curves under different voltage scanning directions that are similar to other solar cells using highly doped Spiro-OMeTAD as the HTL, the hysteresis in MeBz/KOHbased PQDSCs was substantially suppressed compared to that in MeBz-based devices (Supplementary Fig. 21)<sup>50</sup>. Besides alkalis, it has been reported that acids also have the potential to catalyze ester hydrolysis<sup>47</sup>. Nevertheless, PQDSCs fabricated based on MeBz/acetic acid interlayer rinsing only showed a PCE of up to 13.56% (Supplementary Fig. 22), likely due to the acid disrupting the dynamic equilibrium of X-type ligand pairs on the PQD surface, thus accelerating the structure disruption of perovskite lattice<sup>51</sup>. It is worth noting that although the ester hydrolysis in alkaline environments proceeds via the nucleophilic attack by OH<sup>-</sup> ions, the presence of water molecules is essential, as it serves as the medium that enables OH- dissociation and facilitates the overall hydrolysis process. Without the participation of water, the ester antisolvent rinsing of PQD solids cannot effectively trigger X-site ligand exchange, as demonstrated in Supplementary Fig. 23 and Supplementary Note 3. Figure 3d and Supplementary Fig. 24 present the incident photon-to-electron conversion efficiency (IPCE) spectra of PQDSCs. The integrated photocurrent densities of 18.65 mA cm<sup>-2</sup> and 19.05 mA cm<sup>-2</sup> were recorded for MeBz- and MeBz/ KOH-based PQDSCs, respectively, aligning well with the  $J_{sc}$  extracted from the J-V curves. Moreover, as depicted in Fig. 3e, the stabilized efficiency of 17.85% for MeBz/KOH-based PQDSCs matches their PCE values extracted from J-V curves. According to Fig. 3f, it is noteworthy that the champion PCE of our PQDSCs is the highest value among solar cells fabricated with hybrid A-site PQDs. To further validate the potential of the AAAH-based ligand exchange for large-area photovoltaic applications, we fabricated 1 cm<sup>2</sup> solar cells (Supplementary Fig. 25), which achieved a champion PCE of 15.60%, highlighting the promising scalability of this strategy.

Following the confirmation that the AAAH strategy effectively improved the efficiency of solar cells, we proceeded to investigate the stability of the PQDSC devices. We first tested the shelf life of unencapsulated PQDSCs under ambient conditions with an RH of 20–30%, following the ISOS-D-1 protocol<sup>52</sup>. Figure 3g displays the normalized

PCE variations over aging time, with the corresponding pristine *J–V* curves in Supplementary Fig. 26. It can be observed that after 20 days of aging, MeBz-based PQDSC lost over ~40% of its initial PCE. In contrast, MeBz/KOH-based PQDSC could maintain ~82% of the initial efficiency after 30 days of aging.

Moreover, the continuous operational stability of a solar cell is crucial for evaluating the overall performance of the device in practical applications. We therefore conducted photostability measurements on PQD solid films and unencapsulated PQDSCs53. The suppressed peak splitting in steady-state PL spectra and grazing-incidence XRD pattern demonstrated that the light-induced phase segregation in neat MeBz-based hybrid FA<sub>x</sub>Cs<sub>1-x</sub>PbI<sub>3</sub> PQDs could be significantly inhibited by a more efficient ligand exchange using the AAAH strategy (Supplementary Fig. 27)36,54. Moreover, as shown in Fig. 3h, MeBz/KOHbased PQDSC lost as low as 10% of its PCE after 400 h of continuous output at its maximum power under 100 mW cm<sup>-2</sup> illumination, while MeBz-based PQDSC retained only about 60% of its efficiency after tracking its maximum power points for 200 h. The improved storage and operational stability of PQDSCs could be attributed to the more complete capping with hydrophobic BZA ligands on the PQD surface, inhibiting vacancy-triggered moisture/oxygen penetration and ion migration<sup>55</sup>.

# Microphysical and optoelectronic properties of PQD lightabsorbing layers

The aforementioned studies have demonstrated that the pristine longchain OA ligands on the PQD surface could be sufficiently substituted with short anionic ligands through the AAAH strategy. Accordingly, we measured the trap density of states (tDOS) using thermal admittance spectroscopy on devices fabricated from PQD solids without posttreatment A-site ligand exchange, as shown in Supplementary Fig. 28. The MeBz/KOH-based PQDSCs exhibited a notably lower trap density compared to the neat MeBz-based control device, especially in the shallow trap region of 0.30-0.37 eV. This result indicates that the hydrolyzed BZA Lewis base ligands effectively passivate iodide vacancies on the POD surface, contributing to the suppression of nonradiative recombination pathways in photovoltaic devices. In the following section, we will delve into the microscopic surface physical and optoelectronic properties of PQD solid films prepared via a comprehensive two-step sequential X- and A-sites ligand exchange as similar to the light-absorbing layer in PQDSCs, aiming at elucidating the mechanisms underlying the enhancement in photovoltaic performance.

FT-IR spectra (Supplementary Fig. 29) verified that the introduced short conductive PhAD<sup>+</sup> ligands could effectively substitute the pristine long-chain insulating OAm+ ligands on the A-site of the PQD surface during 2-PeOH/PhAD+ post-treatment without affecting the FA+ components and the interlayer exchanged X-site BZA ligands. PQD solid films of a certain thickness have been reported to undergo significant volume shrinkage upon antisolvent rinsing, which is caused by the drastic loss of the pristine long-chain ligands, bringing adjacent PQDs into closer proximity<sup>56</sup>. Nevertheless, once these PQDs draw too close to agglomerate, it leads to delamination between the top and bottom layers, and severely deteriorates charge transport (Supplementary Fig. 30a). Therefore, to investigate the depth-dependent structural characteristics of 2-PeOH/PhAD+ post-treated PQD solid films, we employed the grazing-incidence wide-angle X-ray scattering (GIWAXS) technique at incident angles of 0.2° and 0.8°, corresponding to probe depths of approximately 2 nm (surface region) and 100 nm (bulk region), respectively. This technique enabled the collection of two-dimensional (2D) Bragg reflections (e.g., spots, arcs, or rings) from specific lattice planes, thus providing detailed crystallographic information within PQD solid films<sup>57,58</sup>. As shown in Fig. 4a-d, at an incident angle of 0.8°, samples exhibited clear ring scattering signals at vectors (q) of 1.012, 1.432, and 2.021  $\mathring{A}^{-1}$ , corresponding to the (110), (111), and

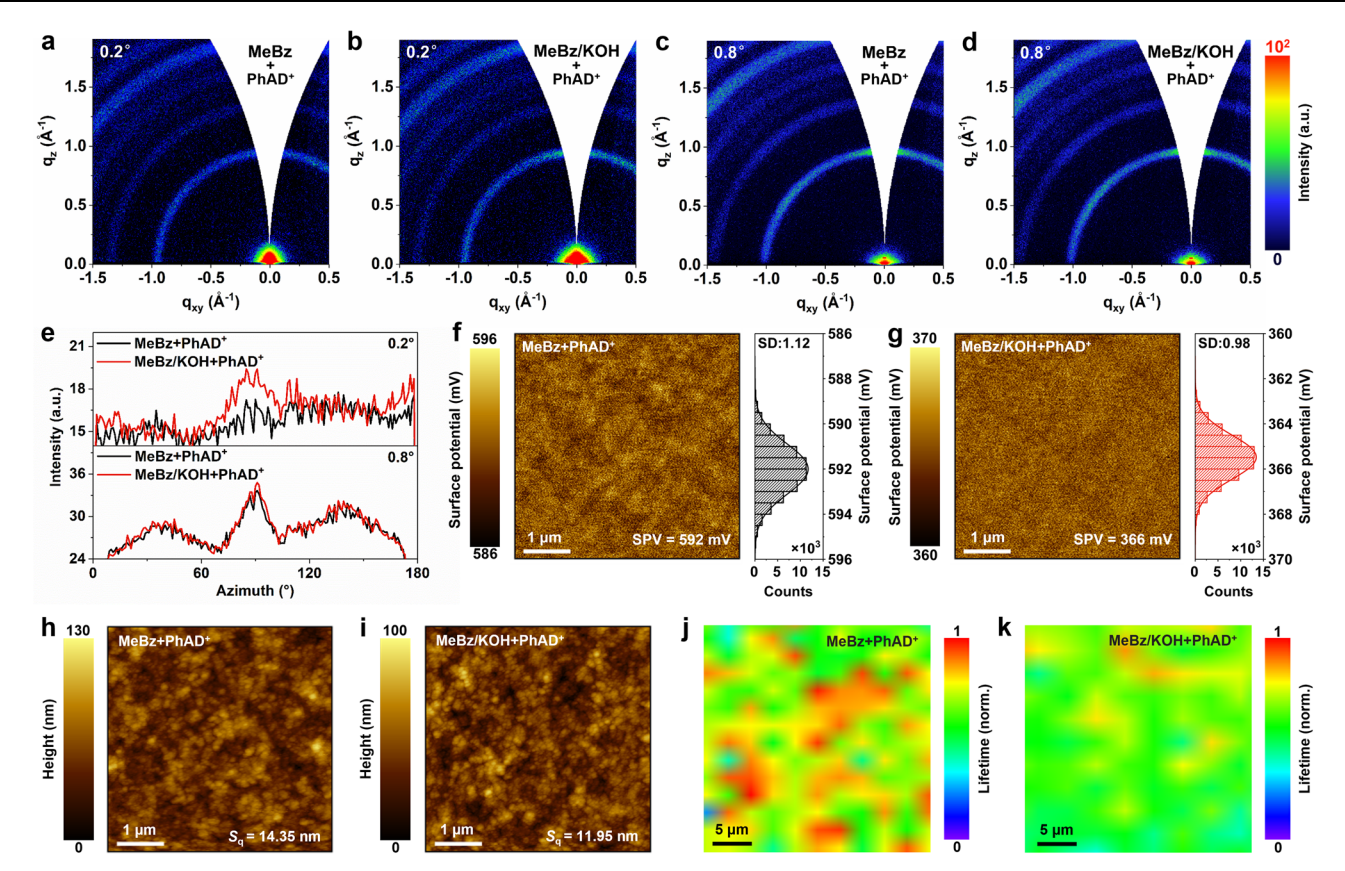


**Fig. 4** | **Effects of AAAH strategy on microphysical and optoelectronic properties of PQD light-absorbing layers.** 2D GIWAXS pattern of 2-PeOH/PhAD<sup>+</sup> post-treated MeBz- (**a**, **c**) and MeBz/KOH- (**b**, **d**) based PQD solid films at incident angles of 0.2° (**a**, **b**) and 0.8° (**c**, **d**). **e** Azimuthally integrated GIWAXS intensity at incident

angles of 0.2° and 0.8° of 2-PeOH/PhAD<sup>+</sup> post-treated MeBz- and MeBz/KOH-based PQD solid films. KPFM images and corresponding surface potential distributions (**f**, **g**), AFM images (**h**, **i**), and 2D pseudo-color PL lifetime maps (**j**, **k**) of 2-PeOH/PhAD<sup>+</sup> post-treated MeBz- (**f**, **h**, **j**) and MeBz/KOH- (**g**, **i**, **k**) based PQD solid films.

(220) lattice planes, respectively. However, when the incident angle was reduced to 0.2°, the q values showed a slight increase (Supplementary Fig. 30b. c), indicating compressive strain at the top of the light-absorbing layer, probably originating from the removal of pristine ligands from the PQD surface<sup>58</sup>. Figure 4e illustrates that at an incident angle of 0.8°, the MeBz/KOH-based PQD solid film merely exhibited a slightly higher integrated intensity than the MeBz-based sample at an azimuthal angle of 90°, indicating that the crystallographic orientations within the bulk of both samples are comparably well-defined. In contrast, when the incident angle was as small as 0.2°, the azimuthal integrated intensity at 90° of MeBz/KOH-based PQD solid films was significantly stronger than that of the MeBz-based sample, almost as high as that of the sample without 2-PeOH/PhAD+ post-treatment (Supplementary Fig. 30d, e). These results suggested that the AAAH strategy effectively stabilizes homogeneous crystallographic orientations throughout the depth of the light-absorbing layer by forming a more integral surface BZA ligand capping.

Kelvin probe force microscopy (KPFM) was employed to analyze the surface potential of the PQD light-absorbing layer<sup>59</sup>. As illustrated in Fig. 4f, g, after being post-treated with 2-PeOH/PhAD<sup>+</sup>, MeBz/KOH-based PQD solid film displayed a lower surface potential and a more uniform surface potential distribution compared to the MeBz-based sample. This demonstrates a greater number of phenyl electron donors hydrolyzed from MeBz effectively coordinate to the PQD surface, effectively improving the surface capping integrity and electronic properties of PQDs. In addition, atomic force microscopy (AFM) images revealed that after 2-PeOH/PhAD<sup>+</sup> post-treatment, MeBz/KOH-based PQDs exhibited a clearer particle assembly morphology than the MeBz-based PQDs (Fig. 4h, i). Moreover, the root-mean-square roughness ( $S_{\Omega}$ ) of MeBz/KOH-based PQD solid film ( $S_{\Omega}$ : 11.95 nm) was

lower than that of the MeBz-based sample ( $S_q$ : 14.35 nm), confirming a smoother surface.

We proceeded to perform PL lifetime mapping tests on POD solid films with 2-PeOH/PhAD+ post-treatment to gain further insights into the particle status and photophysical behavior within the PQD lightabsorbing layer 60,61. As shown in Supplementary Fig. 31a, b, the overall lifetime of MeBz/KOH-based PQD solid film (average 6192.47 ps) was significantly longer than that of the MeBz-based sample (average 3825.73 ps). Figure 4j, k present normalized 2D pseudo-color maps of the PQD solid films, where the MeBz-based sample exhibited multiple scattered bright spots with lifetimes significantly exceeding the average, likely due to the formation of large-sized nanocrystal agglomerates<sup>62</sup>. After splitting the PL lifetime components by a bi-exponential function (Supplementary Fig. 31c, d), it was found that the MeBz-based sample exhibited massive carrier capture sites in the fast decay region, representing the nonradiative recombination. In contrast, both the overall and split lifetime distributions of the MeBz/KOH-based PQD solid film were more uniform, indicating that the AAAH-based ligand exchange effectively mitigated the aggregations of adjacent PQDs. Furthermore, the more ordered and homogeneous stacking of MeBz/KOH-based PQDs on the substrate than neat MeBz-based counterparts after 2-PeOH/PhAD<sup>+</sup> post-treatment can also be visualized in the scanning electron microscopy (SEM) images (Supplementary Fig. 32).

# Charge carrier extraction and recombination dynamics within PQDSCs

Optoelectronic properties of the light-absorbing layer reflect carrier generation and transport, which are critical determinants of photovoltaic performance. Accordingly, we further analyzed charge carrier

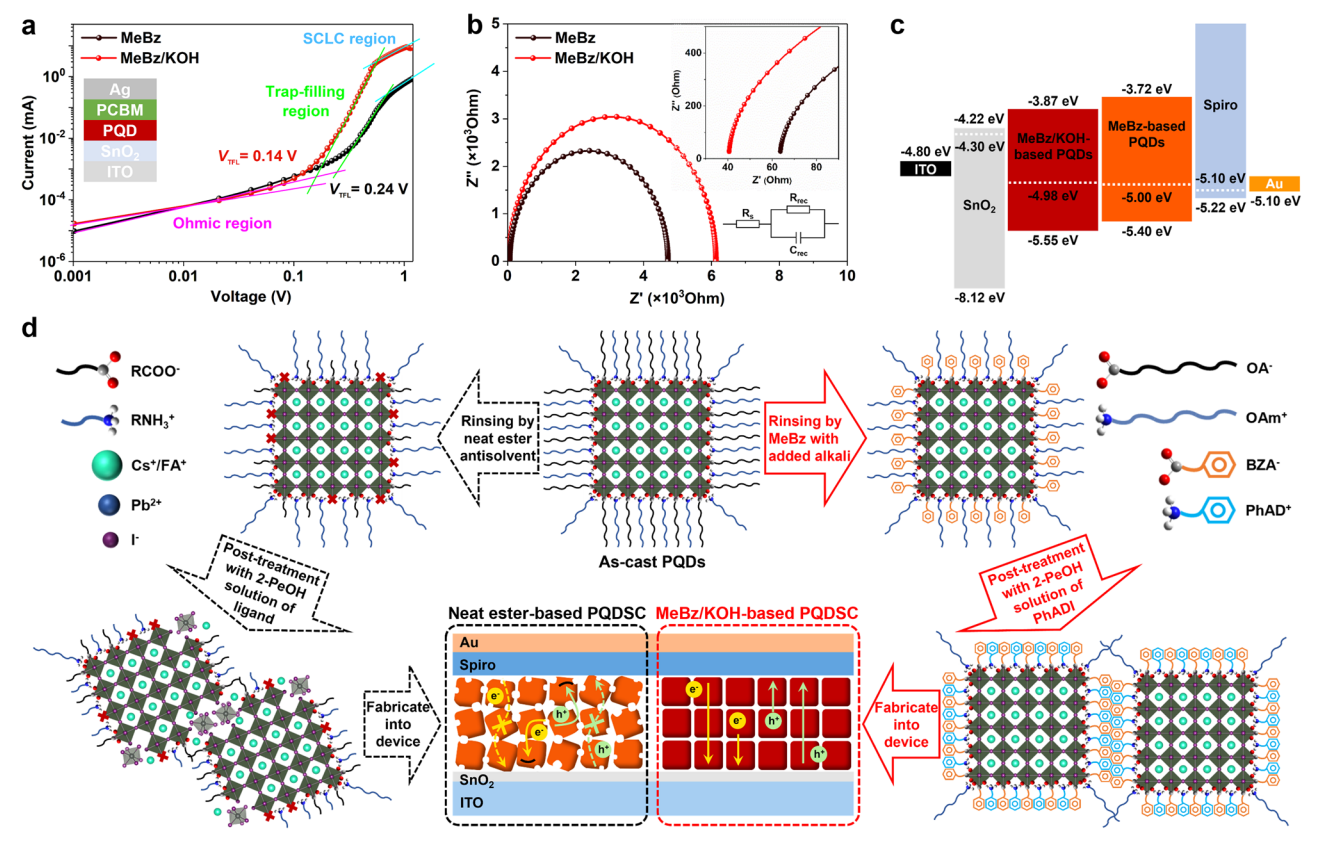


**Fig. 5** | **Effects of AAAH strategy on charge extraction and recombination of PQDSCs. a** SCLC curves of MeBz- and MeBz/KOH-based electron-only devices. Nyquist plots (**b**), energy level diagram of functional layers (**c**) of MeBz- and MeBz/

KOH-based PQDSCs. **d** Schematic diagrams of charge carrier dynamics within PQDSCs fabricated with neat ester antisolvent interlayer rinsing (neat ester-based PQDSCs) and MeBz/KOH-based AAAH interlayer ligand exchange.

kinetics in PQDSC devices. Space charge-limited current (SCLC) measurements were conducted on the electron-only devices with a capacitor-like ITO/SnO $_2$ /PQDs/PCBM/Ag structure to quantify the trap density ( $N_{\rm trap}$ ) within the PQD light-absorbing layer (Fig. 5a).  $N_{\rm trap}$  was derived using the following Eq. 3,

$$N_{\text{trap}} = \frac{2\varepsilon_0 \varepsilon_r V_{\text{TFL}}}{eI^2}$$
 (3)

Where  $V_{\rm TFL}$  is the trap-filled limit voltage, L is the active layer thickness,  $\varepsilon_0$  and  $\varepsilon_{\rm r}$  denote the vacuum permittivity and relative dielectric constant of the active layer, respectively<sup>63</sup>. The  $V_{\rm TFL}$  values for MeBz and MeBz/KOH-based devices were determined to be 0.24 V and 0.14 V, corresponding to the calculated  $N_{\rm trap}$  of  $3.26 \times 10^{15} \, {\rm cm^{-3}}$  and  $1.9 \times 10^{15} \, {\rm cm^{-3}}$ , respectively, indicating that trap states were reduced in the MeBz/KOH-based PQD light-absorbing layer. Additionally, electron mobility ( $\mu_{\rm e}$ ) of the PQD light-absorbing layer was also calculated from the SCLC data using the following Eq. 4,

$$\mu_{\rm e} = \frac{8J_{\rm D}L^3}{9\varepsilon_0\varepsilon_{\rm r}V^2} \tag{4}$$

Where  $J_{\rm D}$  is the dark current density in the SCLC region, and V is the applied voltage<sup>35</sup>. The MeBz/KOH-based device exhibited significantly enhanced  $\mu_{\rm e}$  of  $2.85\times 10^{-4}\,{\rm cm^2\,V^1\,s^{-1}}$  compared to that of  $0.73\times 10^{-4}\,{\rm cm^2\,V^{-1}\,s^{-1}}$  for the MeBz-based device, which implies a better electron transport within the MeBz/KOH-based PQD light-absorbing layer.

Further analysis of the charge recombination dynamics within a complete PQDSC device was performed by examining the light intensity-dependent  $V_{\rm OC}$  (Supplementary Fig. 33a). The  $V_{\rm OC}$  could be

approximated as a linear function of light intensity, modeled by the following Eq. 5,

$$V_{\rm OC} = \frac{nkT}{q} \ln \left( \frac{J_{\rm ph}}{J_0} + 1 \right) \tag{5}$$

Where n, k, T,  $J_{\rm ph}$ , and  $J_0$  are the diode ideality factor, Boltzmann constant, Kelvin temperature, photocurrent density, and reverse saturation current density, respectively<sup>64</sup>. The slope of the linear relationship, indicative of diode behavior, decreased from 2.07 kT/q in MeBz-based PQDSC to 1.45 kT/q in MeBz/KOH-based device, probably due to suppressed trap-assisted charge recombination. Electrochemical impedance spectroscopy (EIS) was performed to further elucidate charge transport and recombination performance within PQDSCs. Figure 5b shows the Nyquist plots and the corresponding equivalent circuit model, with the low- and high-frequency regimes of the semicircles revealing the recombination resistance ( $R_{rec}$ ) and the charge transport resistance ( $R_{ct}$ ), respectively. Compared to the MeBzbased PQDSC with an  $R_{\rm ct}$  of 63.7  $\Omega$  and an  $R_{\rm rec}$  of 4.72 k $\Omega$ , the MeBz/ KOH-based sample exhibited a smaller  $R_{ct}$  of 40.6  $\Omega$  and a larger  $R_{rec}$  of 6.13 kΩ, suggesting more efficient charge transport and reduced interfacial recombination<sup>65,66</sup>. As shown in Supplementary Fig. 33b and Supplementary Note 4, to elucidate the mechanisms behind reduced interfacial charge recombination, Mott-Schottky analysis reveals that the MeBz/KOH-based PQDSCs exhibit a higher built-in potential (1.09 V versus 1.07 V) and a significantly lower interfacial carrier density  $(7.28 \times 10^{16} \text{ cm}^{-3} \text{ versus } 1.06 \times 10^{17} \text{ cm}^{-3})$  compared to the neat MeBz-based devices. These align well with the higher  $V_{\rm OC}$  and FF values for MeBz/KOH-based PQDSCs. Moreover, transient photovoltage (TPV) measurements further show a significantly longer carrier lifetime of 4.44 ms in the MeBz/KOH-based devices compared to that of

1.46 ms in the MeBz-based counterparts (Supplementary Fig. 33c). These results further confirm suppressed charge recombination and improved charge extraction within the device fabricated using the AAAH strategy. Ultraviolet photoelectron spectroscopy (UPS) was employed to assess the energy levels of the functional layers in the PQDSC. As depicted in Fig. 5c, the slight upward shift of Fermi level in MeBz/KOH-based PQD solids is likely attributed to the enhanced surface capping of BZA electron-donor ligands that reduces surface potential, as measured by KPFM (Fig. 4f, g). Moreover, the calculated conduction and valence band positions of the MeBz/KOH-based PQD solid film exhibited a downward shift relative to the MeBz-based sample, aligning more closely with the measured conduction band maximum of SnO<sub>2</sub> (Supplementary Fig. 34). This promotes efficient interfacial electron transport and is consistent with the enhanced carrier extraction dynamics observed in the PQDSC devices, as evidenced by the EIS and Mott-Schottky measurements<sup>63,67</sup>.

In addition to MeBz, we also incorporated KOH into other ester antisolvents, especially MeOAc and EtOAc, to optimize interlayer anionic ligand exchange of FA<sub>x</sub>Cs<sub>1-x</sub>PbI<sub>3</sub> PQD solid films. As expected, the resulting PQDSCs outperformed those fabricated via conventional neat ester antisolvent rinsing. Besides, we integrated the AAAH-based interlayer anionic ligand exchange with different previously reported post-treatment cationic ligand exchange, such as FA<sup>+</sup> and PEA<sup>+</sup>, achieving improved PQDSC performance compared to the conventional intralayer neat antisolvent rinsing coupled with the corresponding post-treatment approach. Furthermore, we validated the applicability of the AAAH strategy to PQD solids of different compositions, such as CsPbI<sub>3</sub>, with the resulting PQDSCs exhibiting enhanced PCEs relative to conventional devices. As shown in Supplementary Fig. 35, these findings highlight both the universality and feasibility of the AAAH strategy in manufacturing high-performing PQDSCs.

In light of the aforementioned insights into charge carrier dynamics in PQD solid films and solar cells, we propose a model to comprehensively elucidate the role of AAAH strategy in fabricating high-performing photovoltaic devices (Fig. 5d). POD lattices in the model were expanded from the primitive cell with coordinates shown in Supplementary Data 2. During the layer-by-layer deposition of PQD solid films, conventional interlayer rinsing using neat ester antisolvents, such as MeOAc or MeBz, encounters substantial thermodynamic and kinetic barriers to hydrolysis, predominantly leading to the direct dissociation of pristine OA ligands from the X-site of PQD surface. This process would generate numerous carrier-trapping defects and induce PQD agglomerations after the post-treatment exchanging of A-site pristine OAm+ ligands, consequently deteriorating charge extraction within solar cells. In contrast, the AAAH strategy involves interlayer rinsing of PQD solid films utilizing ester antisolvents with incorporated alkalis (especially MeBz with added KOH), allowing sufficient substitution of pristine long-chain OA ligands with short anionic ligands due to the significantly lowered energy thresholds for ester hydrolysis. This strategy maintains the integrity of conductive capping on the PQD surface and the independence of adjacent nanoparticles after subsequent A-site ligand exchange, ensuring the assembled light-absorbing layers featuring superior optoelectronic properties, homogeneous crystallographic orientations, and favorable energy level alignments, substantially suppressing carrier recombination and vacancy-mediated ion migration within PQDSCs, consequently enhancing their efficiency and stability.

#### Discussion

In summary, we have demonstrated an efficient AAAH strategy for enriching the conductive capping of PQD surfaces, enabling the fabrication of high-performance solar cells. Through identifying MeBz as the preferred antisolvent and establishing proper alkaline environments via KOH incorporation to promote its hydrolysis under ambient conditions, the pristine long-chain OA ligands on the PQD surface

were rapidly substituted by the hydrolyzed short BZA ligands in 2-fold the conventional number. This AAAH-based ligand exchange effectively diminished defects in the assembled light-absorbing layers, homogenized crystallographic orientations, suppressed PQD agglomerations, and optimized energy-level alignment. Consequently, it enabled PQDSCs to achieve a PCE of 18.37% (certified 18.30%), the highest reported for solar cells fabricated with hybrid A-site PQDs. Moreover, the dense ligand coverage on PQDs imparted by the AAAH strategy enhanced both storage and operational stability of solar cells. The high photovoltaic performance was attributed to the simultaneous suppression of trap-assisted recombination and enhancement of charge extraction. This work offers a versatile and practical route for precisely modulating the PQD surface ligand chemistry, advancing the performance of next-generation photovoltaics and other optoelectronic devices.

#### Methods

#### **Materials**

Cesium carbonate (Cs<sub>2</sub>CO<sub>3</sub>, 99.99% (metals basis)), oleic acid (OA, 90% (tech. grade)), oleylamine (OAm, 80-90% (tech. grade)), methyl acetate (MeOAc, 99.5% (anhydrous)), ethyl acetate (EtOAc, 99.8% (anhydrous)), ethyl cinnamate (EtCa, 98%), methyl formate (MeFo, 99% (anhydrous)), n-hexane (>99% (GC)) and n-octane (>99% (GC)), were purchased from Aladdin. 1-octadecene (ODE, tech. 90.0%), 2-pentanol (2-PeOH, 99%), chlorobenzene (CB, 99.9% (ACS)), methyl methanesulfonate (MMS, 99%), Methyl benzenesulfonate (MeBzSO<sub>3</sub>, 98%), methyl formate (EtFo, 97%), methyl benzoate (MeBz, 99%) and tin (IV) dioxide (SnO<sub>2</sub>, 15% in H<sub>2</sub>O colloidal dispersion) were purchased from Alfa Aesar. Formamidinium iodide (FAI, ≥99.5%), lead iodide (PbI<sub>2</sub>, 99%), 2,2′,7,7′-tetrakis (N,N-di-p-methoxyphenylamine) -9,9'spirobifluorene (Spiro-OMeTAD, ≥99.9%), lithium bis(trifluoromethylsulfonyl)imide (Li-TFSI), benzamidinium iodide (PhADI, 98%), and tris(2-(1H-pyrazol-1-yl)-4-tert-butylpyridine)-cobalt(III)Tris (bis(trifluoromethylsulfonyl)imide)) (FK 209) were purchased from Xi'an Yuri Solar. Acetonitrile (ACN, 99.8% (anhydrous)) and 4-tertbutylpyridine (4-TBP, 96%) were obtained from Sigma-Aldrich. Potassium trimethylsilanolate(Me<sub>3</sub>SiOK, 98%), potassium hydroxide (KOH, 85%(GR)), potassium carbonate (K<sub>2</sub>CO<sub>3</sub>, 99%) were purchased from Innochem. Toluene (TOL, 99% (AR)) was purchased from Xilong Scientific. All reagents were used as received without further purification.

## Synthesis of CsPbI<sub>3</sub> PQDs

 $Pbl_2$  (0.922 g) and ODE (50 mL) were placed into a 250 mL 3-neck flask, and the mixture was degassed at 120 °C under a vacuum for 1 h. Subsequently, OA and OAm (5 mL each) were injected into the flask under an  $N_2$  atmosphere, followed by vacuum degassing until all precursors were fully dissolved. The temperature was then raised to 180 °C under continuous  $N_2$  flow, at which point the 100 °C preheated Cs-OA precursor (4 mL) was swiftly injected into the flask. After 5 s, the flask was rapidly immersed in an ice-water bath to cool the temperature down. The preparation of Cs-OA precursor involved loading  $Cs_2CO_3$  (0.611 g), OA (1.88 mL), and ODE (30 mL) into a three-necked flask. The mixture was degassed under a vacuum at 120 °C for 1 h, after which the temperature was heated to 150 °C under a continuous  $N_2$  flow until the  $Cs_2CO_3$  was completely dissolved, resulting in a clear solution.

## Preparation of FA<sub>x</sub>Cs<sub>1-x</sub>PbI<sub>3</sub> PQDs

 $FA_xCs_{1-x}Pbl_3$  PQDs were prepared by post-synthetic cation exchange of CsPbl<sub>3</sub> PQDs. During the 1st purification process, 35 mL MeOAc antisolvent was added to 15 mL as-synthesized CsPbl<sub>3</sub> PQDs, followed by centrifuging at 8000 rpm (6400 g) for 5 min. After that, the supernatant was discarded, and the PQD precipitate was collected and dissolved in hexane at a concentration of 25 mg mL<sup>-1</sup> for subsequent cation exchange. During the 2nd purification process, ACN and TOL mixture (2:3, v/v) solution of FAI (FAI-ACN/TOL, at a concentration of

1.5 mg mL<sup>-1</sup>) was added in a 1:1 volume ratio to the I<sup>st</sup> purified hexane solution of PQDs to trigger the cation exchange between Cs<sup>+</sup> and FA<sup>+</sup>, then the mixture was swiftly centrifuged at  $8000 \, \text{rpm} \, (6400 \, g)$  for 5 min. Afterward, the obtained FA<sub>x</sub>Cs<sub>1-x</sub>PbI<sub>3</sub> PQD precipitate was redispersed in hexane (5 mL) and stored overnight in a refrigerator. The stoichiometry of FA<sup>+</sup> in this study was determined to be 0.47 according to Vegard's law. All purification processes of PQDs were conducted under ambient conditions. The purified PQDs were centrifuged at  $4000 \, \text{rpm} \, (1600 \, g)$  for 5 min and vacuum dried before use.

## Deposition of PQD solid films and assembly of lightabsorbing layers

The octane solution of PQDs (~85 mg mL<sup>-1</sup>) was spin-coated on the substrate at 1000 rpm for 10 s and then 2000 rpm for 20 s to deposit one layer of the "as-cast" PQD solid film. After that, alternative ester antisolvents including MMS, MeBzSO<sub>3</sub>, MeFo, EtFo, MeOAc, MeBz, EtOAc, and EtCa with or without dissolved alkalis were pipetted onto the as-cast PQD solid film for ~5 s, followed by spin-drying at 4000 rpm for 60 s, then rinsing again with the same neat ester antisolvent for ~2 s. For the assembly of light-absorbing layers, the above process was repeated 4-5 times to form a thick solid film (500-600 nm), which was subsequently treated with the 2-PeOH solution of PhADI (2-PeOH/ PhADI, 0.5 mg mL<sup>-1</sup>) for ~5 s and then spin-dried at 2000 rpm for 60 s, followed by rinsing the solid film with neat EtOAc. The modified ester antisolvent was prepared by adding 1 mg alkali powder, such as Me<sub>3</sub>SiOK, K<sub>2</sub>CO<sub>3</sub>, KOH, and NaOH, into 1 mL of ester and sonicating for 40 min to prepare a saturated solution. Excess solids were removed by centrifugation at 8000 rpm (6400 g) for 5 min. The 2-PeOH/PhADI was prepared by sonicating the PhADI powder in 2-PeOH until the solids were completely dissolved. All solid film preparation processes were carried out under ambient conditions at a relative humidity (RH) of 30-40%.

#### Material characterization

The X-ray diffraction (XRD) pattern was measured using an X-ray diffractometer (D8 Advance, Bruker) with Cu K $\alpha$  radiation ( $\lambda = 1.54 \text{ Å}$ ), covering a scanning range of diffraction angles from 5° to 50°. Grazingincidence wide-angle X-ray scattering (GIWAXS) measurement was performed using a SAXS/WAXS laboratory beamline (Xeuss 3.0, XENOCS) equipped with a Cu K $\alpha$ 2 X-ray source (8.028 keV, 1.54 Å), and the diffraction patterns were collected by a detector (Pilatus3 1M, Dectris). The exposure time for each PQD solid was kept at 120 s during measurement to maximize the signal-to-noise ratio. The thickness of PQD solid films was measured by a step profiler (Dektak XT, Bruker). The AFM and KPFM results were measured using an atomic force microscope (FMNanoview 1000), a Pt-coated Si tip (Model HA-FM/Pt/ 15) with a spring constant  $(k) = 3.5 \text{ Nm}^{-1}$  was employed. Scans were performed over 5 µm at 256 pixels and 1 Hz frequency in a dual-pass setup, the first pass to record topography and the second to measure the contact-potential difference (CPD) in tapping mode. The work function of the Pt tip was calibrated by measuring the CPD relative to a freshly cleaved highly oriented pyrolytic graphite (HOPG) with a standard work function of 4.6 eV. All measurements were done in ambient conditions under indoor lighting. FT-IR spectroscopy was conducted using a Nicolet 6700 FT-IR Spectrometer in transmittance mode. The absorption spectra were recorded using an Ultravioletvisible (UV-Vis) spectrophotometer (UV-2600, SHIMADZU). Steadystate photoluminescence (PL) spectra were recorded using a spectrofluorometer (Puguangweishi Technology Co., Ltd) under a 375 nm monochromatic excitation. Time-resolved photoluminescence (TRPL) decay spectra were measured using a transient fluorescence spectrometer (FLS1000, Edinburgh) equipped with a picosecond diode laser with a 374 nm excitation light. Fluence-dependent TRPL spectra were acquired by exciting the PQD solid films with a 405 nm laser diode (PDL 800-D, PicoQuant) operating at a 2.5 MHz repetition rate under varying fluences. The emitted signal was passed through a monochromator to select the desired wavelength and detected using a photomultiplier tube (PMA Hybrid 50, PicoQuant), with timing controlled by a time-correlated single photon counting module (Harp 300 Picosecond Event Timer, PicoQuant). PL lifetime mapping images were captured with a microscopic fluorescence lifetime imaging system (OmniFluo-FLIM, Zolix Instruments Co. Ltd.) equipped with a timedependent single photon counter (TCSPC), a 375 nm picosecond pulsed laser was employed to excite the fluorescence of the PQDs and a 100X objective with a spatial resolution of ≤1 µm was adopted to carry out the imaging. The morphology of perovskite quantum dots (PQDs) was characterized using a transmission electron microscope (JEM-2100, JEOL) at an accelerating voltage of 200 kV. X-ray photoelectron spectroscopy (XPS) and ultraviolet photoelectron spectroscopy (UPS) measurements were performed using a spectrometer (ESCALAB 250Xi, Thermo) with excitation using an X-ray and He I (21.22 eV) UV-light source, respectively. The N 1s and O 1s core-level XPS spectra of the samples were deconvoluted using a sum of Lorentzian and Gaussian functions. The fitting was performed with  $\chi^2$ values between 0.95 and 1.1 to ensure reliability. <sup>1</sup>H NMR spectra were collected on an NMR spectrometer (AVANCE III 600 M, Bruker). Raman spectra were collected on a Renishaw 2000 microscope equipped with a 785 nm laser to avoid excitation of the fluorescence signal. The conductivity of PQD solids was recorded under dark conditions, based on devices with a structure of ITO/PQDs/Au. The conductivity value was calculated by the following Eq. 6,

$$J = \sigma V / L \tag{6}$$

Where J, V,  $\sigma$ , and L are current density, applied voltage, conductivity, and film thickness, respectively.

#### **Fabrication of solar cells**

The ITO glass substrate underwent sequential washing procedures using detergent, deionized water, and ethanol. After that, the substrate was subjected to UV-ozone treatment for 20 min to enhance surface wettability and eliminate organic contaminants. A SnO<sub>2</sub> nanoparticle solution (2.67% concentration, diluted with deionized water) was then spin-coated onto the ITO substrate at 4000 rpm for 30 s, followed by annealing at 150 °C for 30 min. The light-absorbing layers were prepared following the above layer-by-layer procedure of PQD solid films. Afterward, the Spiro-OMeTAD solution was spin-coated onto the PQD light-absorbing layer at 4000 rpm for 30 s under ambient conditions at an RH lower than 20%. The Spiro-OMeTAD solution was prepared by dissolving Spiro-OMeTAD in CB at a concentration of 72.3 mg mL<sup>-1</sup>, followed by mixing with 28.8 µL of 4-TBP, 17.5 µL of ACN solution of Li-TFSI (520 mg mL $^{-1}$ ), and 10  $\mu$ L of ACN solution of FK209 (300 mg mL $^{-1}$ ). Finally, a ~ 60 nm thick gold electrode was thermally evaporated onto the top at a rate of 0.5 Å s<sup>-1</sup>, thus completing the solar cell fabrication.

#### Solar cell characterization

The photovoltaic parameters of devices were tested in an  $N_2$  atmosphere. The J-V curves were recorded using the Keithley 2400 digital source meter under AM1.5 G illumination (100 mW cm $^{-2}$ ) provided by a AAA Class solar simulator (71S0503A, SOFN INSTRUMENTS Co., LTD.). The incident light intensity was calibrated using a National Institute of Metrology-certified silicon solar cell, and the working area of an individual cell was  $0.036~\rm cm^2$  defined using a black metallic mask. The voltage scan range is from  $1.3~\rm V$  to  $-0.1~\rm V$ , with a scan speed of  $0.21~\rm V~s^{-1}$  and a dwell time of 20 ms. The incident photon-to-electron conversion efficiency (IPCE) spectra were measured using a quantum efficiency system (QE-R, Enli Technology). The stabilized power output (SPO) was measured by monitoring the photocurrent at the maximum power point (MPP) under continuous illumination (AM1.5 G 100 mW cm $^{-2}$ ). The MPP tracking was carried out in an  $N_2$  atmosphere using a

long-term solar cell stability testing system (PV-S-16, Tianjin Meitong Corp., China) under continuous  $100 \, \mathrm{mW \, cm^{-2}}$  white LED illumination (MT-LED, Tianjin Meitong Corp., China) at  $30 \pm 5 \, ^{\circ}\mathrm{C}$ , with the results automatically recorded by dedicated aging test software. Electrochemical impedance spectroscopy (EIS) measurement was performed in the dark by a compositive electrochemical workstation (CIMPS-pro, Zahner Zennium). The SCLC measurement was conducted using a Keithley 2400 to record the I-V curve of the electron-only device in dark conditions. The  $V_{\mathrm{TFL}}$  was determined by the intersection of the tangent lines between the ohmic and the trap-filling zone.

#### Computational method

First-principles calculations have been carried out using the projected augmented wave (PAW) as implemented in the Vienna Ab Initio Simulation Package (VASP) code to model the binding of perovskite core to a ligand<sup>22</sup>. To save computational effort without compromising the results, individual Cs<sup>+</sup> was chosen to represent the A-site cation in the model. A generalized gradient approximation (GGA) in the form of Perdew-Burke-Ernzerhof (PBE) functionals was employed to describe the exchange-correlation function. A cubic CsPbI<sub>3</sub> {001} surface slab consisting of eight atomic layers within a 2 × 2 supercell was adopted as the substrate, which was separated by a vacuum layer of more than 30 Å to minimize interactions between neighboring slabs<sup>43</sup>. A cut-off energy of 500.0 eV and a gamma-centered K-point mesh of 6 × 6 × 1 were sampled for structural relaxation of the surface slab after convergence tests. The Grimme DFT-D3 corrections were introduced to capture the Van der Waals interactions. The top four layers of the surface slab were fully relaxed using the quasi-Newton algorithm until the energy difference between two successive ionic steps and the Hellmann-Feynman force of each atom converged to 10<sup>-5</sup>eV and 0.02 eV Å<sup>-1</sup>, respectively. While the underlying layers, representing the bulk, were fixed. The binding energy ( $E_{\text{binding}}$ ) of ligands to the surface slab was defined using the following Eq. 7,

$$E_{\text{binding}} = E_{\text{system}} - E_{\text{ligand}} - E_{\text{substrate}}$$
 (7)

where  $E_{\rm system}$  refers to the total energy of the entire system after structure relaxation,  $E_{\rm ligand}$  and  $E_{\rm surface}$  are energies of ligands and surface slab, respectively.

Three-dimensional charge density differences ( $\rho_{\rm diff.}$ ) were calculated using the following Eq. 8,

$$\rho_{\text{diff.}} = \rho_{\text{system}} - \rho_{\text{ligand}} - \rho_{\text{substrate}}$$
 (8)

where  $\rho_{\rm system}$  is the total charge density of the system with ligand binding,  $\rho_{\rm ligand}$  and  $\rho_{\rm substrate}$  are the charge densities of the ligands and the PQD surface slab<sup>16</sup>.

For the investigation of the effect of an alkaline environment on the reaction process of hydrolysis for ester antisolvents, we performed transition state (TS) and intrinsic reaction coordinate (IRC) calculations employing Gaussian 16 set package on account of the density functional theory (DFT). Ground states of molecules were optimized using dispersion-corrected hybrid exchange-correlation B3LYP-D3 (BJ) functionals and the basis set of  $6-31+G^*$ , followed by single-point calculations at  $6-311+G^{**32}$ . The solvent environment was modeled as water using the Polarizable Continuum Model (PCM). The reaction energy barrier ( $E_a$ ) was determined by calculating the energy difference between the transition state and the reactants through the IRC curve.

#### **Reporting summary**

Further information on research design is available in the Nature Research Reporting Summary linked to this article.

# **Data availability**

All data generated in this study are provided in the article and Supplementary Information and the raw data supporting this study are available from the Source Data file. Source data are provided with this paper.

#### References

- Yang, G. & Zhong, H. Organometal halide perovskite quantum dots: synthesis, optical properties, and display applications. *Chin. Chem. Lett.* 27, 1124–1130 (2016).
- Yuan, Z. et al. Interface-assisted cation exchange enables highperformance perovskite LEDs with tunable near-infrared emissions. *Joule* 6, 2423–2436 (2022).
- Hassan, Y. et al. Ligand-engineered bandgap stability in mixedhalide perovskite LEDs. Nature 591, 72–77 (2021).
- Shen, K. et al. Flexible and self-powered photodetector arrays based on all-inorganic CsPbBr<sub>3</sub> quantum dots. Adv. Mater. 32, 2000004 (2020).
- Yakunin, S. et al. Low-threshold amplified spontaneous emission and lasing from colloidal nanocrystals of caesium lead halide perovskites. Nat. Commun. 6, 8056 (2015).
- Swarnkar, A. et al. Quantum dot-induced phase stabilization of α-CsPbl<sub>3</sub> perovskite for high-efficiency photovoltaics. Science 354, 92–95 (2016).
- Zhang, X. L. et al. Conductive colloidal perovskite quantum dot inks towards fast printing of solar cells. Nat. Energy 9, 1378–1387 (2024).
- Song, H. et al. A universal perovskite nanocrystal ink for highperformance optoelectronic devices. Adv. Mater. 35, 2209486 (2023).
- Protesescu, L. et al. Nanocrystals of cesium lead halide perovskites (CsPbX<sub>3</sub>, X = Cl, Br, and I): novel optoelectronic materials showing bright emission with wide color Gamut. Nano Lett. 15, 3692–3696 (2015).
- Rainò, G. et al. Ultra-narrow room-temperature emission from single CsPbBr<sub>3</sub> perovskite quantum dots. Nat. Commun. 13, 2587 (2022).
- Kim, J. et al. Alkali acetate-assisted enhanced electronic coupling in CsPbI<sub>3</sub> perovskite quantum dot solids for improved photovoltaics. Nano Energy 66, 104130 (2019).
- Zhao, Q. et al. Size-dependent lattice structure and confinement properties in CsPbl<sub>3</sub> perovskite nanocrystals: negative surface energy for stabilization. ACS Energ. Lett. 5, 238–247 (2019).
- Jia, D., Chen, J., Zhuang, R., Hua, Y. & Zhang, X. Inhibiting lattice distortion of CsPbI<sub>3</sub> perovskite quantum dots for solar cells with efficiency over 16.6%. *Energy Environ. Sci.* 15, 4201–4212 (2022).
- Jia, D. et al. Surface matrix curing of inorganic CsPbI<sub>3</sub> perovskite quantum dots for solar cells with efficiency over 16%. Energy Environ. Sci. 14, 4599–4609 (2021).
- Zhang, X. et al. Homojunction perovskite quantum dot solar cells with over 1 μm-thick photoactive layer. Adv. Mater. 34, 2105977 (2021).
- Aqoma, H. et al. Alkyl ammonium iodide-based ligand exchange strategy for high-efficiency organic-cation perovskite quantum dot solar cells. Nat. Energy 9, 324–332 (2024).
- Hao, M. et al. Ligand-assisted cation-exchange engineering for high-efficiency colloidal Cs<sub>1-x</sub>FA<sub>x</sub>PbI<sub>3</sub> quantum dot solar cells with reduced phase segregation. *Nat. Energy* 5, 79–88 (2020).
- Li, D. et al. Dual-phase ligand engineering enables 18.21% FAPbl<sub>3</sub> quantum dot solar cells. Adv. Mater. 37, 2417346 (2025).
- Li, H. et al. Buried interface engineering enables efficient and refurbished CsPbl<sub>3</sub> perovskite quantum dot solar cells. Energy Environ. Sci. 18, 972–981 (2025).
- Li, F. et al. Solution-mediated hybrid FAPbl<sub>3</sub> perovskite quantum dots for over 15% efficient solar cell. Adv. Funct. Mater. 33, 2302542 (2023).
- Zhang, X., Huang, H., Zhao, C. & Yuan, J. Surface chemistryengineered perovskite quantum dot photovoltaics. *Chem. Soc. Rev.* 54, 3017–3060 (2025).

- Wang, S. et al. Thermal tolerance of perovskite quantum dots dependent on a-site cation and surface ligand. Nat. Commun. 14, 2216 (2023).
- Zhao, C. Y. et al. Fast organic cation exchange in colloidal perovskite quantum dots toward functional optoelectronic applications. J. Am. Chem. Soc. 146, 4913–4921 (2024).
- Wang, G. et al. Surface matrix-mediated cation exchange of perovskite quantum dots for efficient solar cells. *Angew. Chem. Int. Ed.* 64, 202416747 (2024).
- Li, J. et al. 50-Fold EQE improvement up to 6.27% of solutionprocessed all-inorganic perovskite CsPbBr<sub>3</sub> QLEDs via surface ligand density control. Adv. Mater. 29, 1603885 (2017).
- Hao, N. et al. Flexibly regulated electrochemiluminescence of allinorganic perovskite CsPbBr<sub>3</sub> quantum dots through electron bridge to across interfaces between polar and non-polar solvents. Chin. Chem. Lett. 32, 2861–2864 (2021).
- Ji, Y. et al. Surface engineering enables efficient AgBiS<sub>2</sub> quantum dot solar cells. Nano Lett. 24, 10418–10425 (2024).
- Wheeler, L. M. et al. Targeted ligand-exchange chemistry on cesium lead halide perovskite quantum dots for high-efficiency photovoltaics. J. Am. Chem. Soc. 140, 10504–10513 (2018).
- Sanehira, E. M. et al. Enhanced mobility CsPbl<sub>3</sub> quantum dot arrays for record-efficiency, high-voltage photovoltaic cells. Sci. Adv. 3, eaao4204 (2017).
- 30. Yang, W. et al. Overcoming charge confinement in perovskite quantum dot solar cells. *Adv. Mater.* **35**, 2304533 (2023).
- Lim, S. et al. Monodisperse perovskite colloidal quantum dots enable high-efficiency photovoltaics. ACS Energ. Lett. 6, 2229–2237 (2021).
- Jia, D. et al. Tailoring solvent-mediated ligand exchange for CsPbI<sub>3</sub> perovskite quantum dot solar cells with efficiency exceeding 16.5%.
   Joule 6, 1632–1653 (2022).
- Han, R. et al. Role of methyl acetate in highly reproducible efficient CsPbI<sub>3</sub> perovskite quantum dot solar cells. J. Phys. Chem. C. 125, 8469–8478 (2021).
- 34. Ye, J. et al. Elucidating the role of antisolvents on the surface chemistry and optoelectronic properties of CsPbBr<sub>x</sub>I<sub>3-x</sub> perovskite nanocrystals. *J. Am. Chem.* Soc. **144**, 12102–12115 (2022).
- Jia, D. et al. Dual passivation of CsPbI<sub>3</sub> perovskite nanocrystals with amino acid ligands for efficient quantum dot solar cells. Small 16, 2001772 (2020).
- Jia, D., Chen, J., Zhuang, R., Hua, Y. & Zhang, X. Antisolvent-assisted in-situ cation exchange of perovskite quantum dots for efficient solar cells. Adv. Mater. 35, 2212160 (2023).
- Cho, S. et al. High-voltage and green-emitting perovskite quantum dot solar cells via solvent miscibility-induced solid-state ligand exchange. Chem. Mater. 32, 8808–8818 (2020).
- Zhang, H., Pfeifer, L., Zakeeruddin, S. M., Chu, J. & Grätzel, M. Tailoring passivators for highly efficient and stable perovskite solar cells. Nat. Rev. Chem. 7, 632–652 (2023).
- Koole, R., Liljeroth, P., de Mello Donega, C., Vanmaekelbergh, D. & Meijerink, A. Electronic coupling and exciton energy transfer in CdTe quantum-dot molecules. J. Am. Chem. Soc. 128, 10436–10441 (2006).
- Lu, H. et al. Enhanced photoredox activity of CsPbBr<sub>3</sub> nanocrystals by quantitative colloidal ligand exchange. *J. Chem. Phys.* 151, 204305 (2019).
- Vickers, E. T. et al. Enhancing charge carrier delocalization in perovskite quantum dot solids with energetically aligned conjugated capping ligands. ACS Energ. Lett. 5, 817–825 (2020).
- 42. Wang, T. et al. Phenethylammonium functionalization enhances near-surface carrier diffusion in hybrid perovskites. *J. Am. Chem.* Soc. **142**, 16254–16264 (2020).

- 43. Yang, W. et al. A systematic study of switching, optoelectronics, and gas-sensitive properties of PCF-Graphene-based nanodevices: insights from DFT study. *Carbon Neutral.* **3**, 904–917 (2024).
- 44. Wang, Y. et al. Efficient  $\alpha$ -CsPbI<sub>3</sub> photovoltaics with surface terminated organic cations. *Joule* **2**, 2065–2075 (2018).
- Smock, S. R., Williams, T. J. & Brutchey, R. L. Quantifying the thermodynamics of ligand binding to CsPbBr<sub>3</sub> quantum dots. *Angew. Chem. Int. Ed.* 57, 11711–11715 (2018).
- 46. Xu, J. et al. Anion optimization for bifunctional surface passivation in perovskite solar cells. *Nat. Mater.* **22**, 1507–1514 (2023).
- Afrin, S. & Bollini, P. A transient kinetic analysis of the evolution of a reducible metal oxide towards catalyzing nonoxidative alkanol dehydrogenation. J. Catal. 393, 290–302 (2021).
- Chen, K., Deng, X., Dodekatos, G. & Tuysuz, H. Photocatalytic polymerization of 3,4-Ethylenedioxythiophene over cesium lead iodide perovskite quantum dots. J. Am. Chem. Soc. 139, 12267–12273 (2017).
- Wieliczka, B. M. et al. Probing the origin of the open circuit voltage in perovskite quantum dot photovoltaics. ACS Nano 15, 19334–19344 (2021).
- 50. Liu, P. Y., Wang, W., Liu, S. M., Yang, H. G. & Shao, Z. P. Fundamental understanding of photocurrent hysteresis in perovskite solar cells. *Adv. Energy Mater.* **9**, 1803017 (2019).
- De Roo, J. et al. Highly dynamic ligand binding and light absorption coefficient of cesium lead bromide perovskite nanocrystals. ACS Nano 10, 2071–2081 (2016).
- 52. Khenkin, M. V. et al. Consensus statement for stability assessment and reporting for perovskite photovoltaics based on ISOS procedures. *Nat. Energy* **5**, 35–49 (2020).
- 53. Bai, S. et al. Planar perovskite solar cells with long-term stability using ionic liquid additives. *Nature* **571**, 245–250 (2019).
- 54. Gualdron-Reyes, A. F. et al. Controlling the phase segregation in mixed halide perovskites through nanocrystal size. *ACS Energy Lett.* **4**, 54–62 (2019).
- 55. Du, S. X. et al. Inhibiting perovskite decomposition by a creeperinspired strategy enables efficient and stable perovskite solar cells. *Nat. Commun.* **15**, 5223 (2024).
- Kim, J. et al. Single-step-fabricated perovskite quantum dot photovoltaic absorbers enabled by surface ligand manipulation. *Chem. Eng. J.* 448, 137672 (2022).
- 57. Zhao, X. et al. Regulation of buried interface through the rapid removal of Pbl<sub>2</sub>·DMSO complex for enhancing light stability of perovskite solar cells. ACS Energ. Lett. **9**, 2659–2669 (2024).
- 58. Steele, J. A. et al. How to GIWAXS: grazing incidence wide angle X-Ray Scattering applied to metal halide perovskite thin films. *Adv. Energy Mater.* **13**, 2300760 (2023).
- Lan, Z. N. et al. Cascade reaction in organic hole transport layer enables efficient perovskite solar cells. Angew. Chem. Int. Ed. 63, 202402840 (2024).
- Li, N. et al. Liquid medium annealing for fabricating durable perovskite solar cells with improved reproducibility. Science 373, 561–567 (2021).
- 61. Yang, X. Y. et al. Perovskite hetero-bilayer for efficient charge-transport-layer-free solar cells. *Joule* **6**, 1277–1289 (2022).
- 62. Koley, S., Cui, J., Panfil, Y. E. & Banin, U. Coupled colloidal quantum dot molecules. Acc. Chem. Res. **54**, 1178–1188 (2021).
- 63. Huang, H. et al. 24.8%-efficient planar perovskite solar cells via ligand-engineered TiO<sub>2</sub> deposition. *Joule* **6**, 2186–2202 (2022).
- 64. Hu, L. et al. Flexible and efficient perovskite quantum dot solar cells via hybrid interfacial architecture. *Nat. Commun.* **12**, 466 (2021).
- 65. Yang, Y. et al. Compatible soft-templated deposition and surface molecular bridge construction of SnO<sub>2</sub> enable air-fabricated perovskite solar cells with efficiency exceeding 25.7%. Adv. Energy Mater. 14, 2400416 (2024).

- 66. Ma, P. et al. A novel design for conversion and storage of solar thermal energy into electrical energy using a solar thermoelectric device-coupled supercapacitor. *Carbon Neutral.* **3**, 781–797 (2024).
- Lan, Z. et al. Homogenizing the electron extraction via eliminating low-conductive contacts enables efficient perovskite solar cells with reduced up-scaling losses. Adv. Funct. Mater. 34, 2316591 (2024).

# **Acknowledgements**

This work is supported partially by the National Natural Science Foundation of China (52402255 to D. J., 62404080 to H.Q., 52232008 to M. L., 51972110 to M. L., 52102245 to P. C., 52302250 to X. S., 22409061 to X. Z.), Beijing Natural Science Foundation (Z240024 to P. C.), the Fundamental Research Funds for the Central Universities (2024JC005 to M. L.), the Fundamental Research Funds for the Central Universities (2024JC005 to M. L.), the Fundamental Research Funds for the Central Universities (2024MS037 to D. J., 2024MS034 to H. Q.), the NCEPU "Double First-Class" Program, and the Beijing Nova Program. We thank Mr. Y. Zhao and H. Sun (Zolix Instruments Co. Ltd.) for assisting with PL lifetime mapping measurement and discussion.

# **Author contributions**

M. L. and D. J. conceived the idea and experimental projects. M. L. guided the work as the supervisor. D. J., J. L., and H. Q. were responsible for PQD synthesis, post-synthetic cation exchange, and material characterization. D. J., J. L., K. Z., and F. Y. did solar cell fabrication and device characterization. H. Q. performed TEM measurement. Z. L. conducted AFM and KPFM tests. S. L. conducted fluence-dependent TRPL measurement. L. L., X. Z., H. Y., P. C., P. Z., X. S., and H. L. participated in some material and device characterizations. D. J. conducted DFT calculations and data analysis. D. J. wrote the first version of the manuscript and prepared figures. All authors contributed to discussions and commented on the manuscript, and all authors reviewed the manuscript.

# **Competing interests**

The authors declare no competing interests.

#### **Additional information**

**Supplementary information** The online version contains supplementary material available at https://doi.org/10.1038/s41467-025-63618-5.

**Correspondence** and requests for materials should be addressed to Meicheng Li.

**Peer review information** *Nature Communications* thanks Jian-Yu Yuan, and the other, anonymous, reviewer(s) for their contribution to the peer review of this work. A peer review file is available.

**Reprints and permissions information** is available at http://www.nature.com/reprints

**Publisher's note** Springer Nature remains neutral with regard to jurisdictional claims in published maps and institutional affiliations.

Open Access This article is licensed under a Creative Commons Attribution-NonCommercial-NoDerivatives 4.0 International License, which permits any non-commercial use, sharing, distribution and reproduction in any medium or format, as long as you give appropriate credit to the original author(s) and the source, provide a link to the Creative Commons licence, and indicate if you modified the licensed material. You do not have permission under this licence to share adapted material derived from this article or parts of it. The images or other third party material in this article are included in the article's Creative Commons licence, unless indicated otherwise in a credit line to the material. If material is not included in the article's Creative Commons licence and your intended use is not permitted by statutory regulation or exceeds the permitted use, you will need to obtain permission directly from the copyright holder. To view a copy of this licence, visit <a href="https://creativecommons.org/licenses/by-nc-nd/4.0/">https://creativecommons.org/licenses/by-nc-nd/4.0/</a>.

© The Author(s) 2025